OBSERVATIONS OF THE GALACTIC PLANE AT 960 Mc/s

Thesis by

Robert Woodrow Wilson

In Partial Fulfillment of the Requirements

For the Degree of

Doctor of Philosophy

California Institute of Technology

Pasadena, California

1962

ACKNOWLEDGMENTS

It is with pleasure that I thank:

1) J. G. Bolton, former director of the observatory, for suggesting this project, scheduling the observing time, and working many hours on the original data reduction
2) M. Schmidt, who acted as advisor since the departure of J. G. Bolton, and with whom I have had many valuable discussions
3) L. Davis, who has been my physics department advisor
4) G. J. Stanley, present director of the observatory, who was responsible for the receiver, and has provided much encouragement and support
5) D. E. Harris, who provided receiver calibration data for the single dish receiver, and helpful discussion of supernova remnants
6) A. T. Moffet, who provided E.-W. interferometer and single dish measurements of several sources
7) P. Maltby, who provided receiver calibration data for the N.-S. interferometer observations and data on several sources
8) The various other students and members of the staff who helped with observations
9) The Office of Naval Research, which supports the Caltech Radio Observatory under contract number NONR 220(19)
10) The National Science Foundation, which provided three graduate fellowships
11) The Institute, for providing tuition grants during my last two quarters.

R. W. W.

ABSTRACT

A survey of the radio radiation at 960 Mc/s from the part of the plane of the Galaxy with declination above 48° has been made. 112 discrete sources were found in the region studied. The positions, intensities, and sizes of these sources have been catalogued, and a search for optical identifications made. The broadly distributed radiation is interpreted in terms of a space distribution of ionized hydrogen and of emissivity from synchrotron emission.

I. INTRODUCTION

In studying the Galaxy, astronomers are limited rather severely by the large amounts of obscuring matter in the plane. It is possible to determine the positions and radial velocities accurately for a large number of stars, but most of them are within 2 kpc of the sun. This is a severe limitation, considering that the sun is about 10 kpc from the center of a system whose diameter is about 24 kpc. One help in this problem is to observe external systems like the Andromeda nebula, where we can get a good view of the whole system, and seek hints of what our system is like.

Another help is to observe the Galaxy with radio waves, which can "see" through the obscuring dust. In addition to seeing through obscuring dust, however, radio waves come from a somewhat different class of objects than light waves do. Thus, while ordinary stars produce negligible radio radiation, interstellar hydrogen and cosmic rays produce strong radiation.

Radio observations of the Galaxy date back to the start of radio astronomy in 1931, when Jansky (1) discovered extra-terrestrial radio emission coming from the direction of the galactic center. Since that time, a large part of the effort in radio astronomy has gone into studies of galactic radiation. At first the small antennas and insensitive receivers that were available, coupled with the overwhelming flux density of galactic radiation limited radio astronomy to galactic observations. After the discovery of discrete sources in 1946, by Hey, Parsons and Phillips (2), interferometers and large telescopes capable of discrimi-

nating against the relatively smoothly distributed radiation from the Galaxy were constructed, opening up the field of solar and extra-galactic observations. Although much work has been done in these fields, the importance of radio observations in galactic astronomy has been such that much time has continued to be spent on galactic observations.

The Owens Valley Radio Observatory of the California Institute of Technology has as its principal instrument a two-element variable spacing interferometer made up of two 90' steerable paraboloids. The primary purpose of this instrument is the determination of accurate positions of small diameter sources, and the measuring of their brightness distributions. The survey of the plane of the Galaxy, on which this thesis is based, was done during the initial period of operation after the completion of major construction, when one of the 90' paraboloids was equipped with a 960 Mc/s radiometer. The survey covers all of the plane visible from the observatory, and has a resolution comparable to surveys which are available at other frequencies.

II. GENERAL PROPERTIES OF RADIO TELESCOPES

A radio telescope is an antenna which is adapted for receiving cosmic radio radiation. Before discussing the response of a radio telescope to cosmic radiation, it will be useful to consider a few properties of the radiation itself.

Except for the hydrogen line, the spectrum of the radiation we can receive is limited in extent only by the transmissivity of the earth's atmosphere. The spectrum is thus continuous from 20 or 30 Mc/s, depending on ionospheric conditions, up to about 30,000 Mc/s depending on the amount of water vapor in the air. The radiation is randomly polarized except for a few sources, so that an antenna can receive only half of the radiation incident on it.

We will characterize the intensity of the radiation by its brightness (B_ν) in the vicinity of the frequency ν. Brightness is defined by the relation that the power incident on an area dA, normal to the direction of incidence, from within a solid angle $d\Omega$ in a frequency band of width $d\nu$ is given by:

$$B_\nu dA\, d\Omega\, d\nu \tag{1}$$

In the case of a discrete source we will speak of the flux density of the source (S_ν). S_ν is the power incident from the source per unit area normal to the direction of incidence per unit bandwidth. Thus the power is given by:

$$S_\nu\, dA\, d\nu \tag{2}$$

Comparing with equation 1 we obtain:

$$S_\nu = \int_{\text{Source}} B_\nu \, d\Omega \tag{3}$$

It is implicit in the definition of flux density that we consider only the radiation from the source in question, and avoid the effects of radiation from other sources in about the same direction.

If the source of radiation is a black body of absolute temperature T, the brightness is given by the Raleigh-Jeans formula for radio frequencies:

$$B_\nu = \frac{2k}{c^2}\nu^2 T = \frac{2k}{\lambda^2} T \tag{4}$$

where k = Boltzman's constant, c = the velocity of light, and $\lambda = \frac{c}{\nu}$ = wavelength. Even though little radio radiation originates from sources of the black body type, brightness is often expressed in terms of the equivalent brightness temperature ($T_{b,\nu}$). This brightness temperature will in general be a function of frequency. We will henceforth drop the subscript ν from B, S, and T_b.

Consider a lossless radio telescope in a universe containing one unpolarized point source whose flux density at the antenna is S. As the telescope is oriented in different directions, a direction will be found in which a maximum power P_o is delivered to the receiver. Let us define a system of spherical coordinates centered on the telescope and rotating with it. Let the pole $\theta = 0$ be in the direction of maximum power reception. With the source in the direction $\theta = 0$, the antenna will be collecting the power contained in an area A_o of

wave front from the source where from equation 2:

$$P_o = \frac{S}{2} A_o \Delta\nu \tag{5}$$

The factor of $1/2$ is a result of the antenna's accepting only one mode of polarization. $\Delta\nu$ is the bandwidth over which the power is measured. If the antenna is directed so that the source is in some other position (θ, ϕ), the power received will be less corresponding to a reduced effective area. We will define a function $f(\theta, \phi)$ so that in any direction:

$$P(\theta, \phi) = \frac{S}{2} A_o f(\theta, \phi) \Delta\nu \tag{6}$$

Having found the response of the antenna to a point source, we can find the response to a spread source by convolution. Using equation 3, the result is:

$$P = \frac{A_o \Delta\nu}{2} \int B(\theta, \phi) f(\theta, \phi)\, d\Omega \tag{7}$$

or in terms of brightness temperature using equation 4 we get:

$$P = \frac{A_o k}{\lambda^2} \int T_b(\theta, \phi) f(\theta, \phi)\, d\Omega \tag{8}$$

The power output of an antenna is often referred to in terms of the temperature of a hot resistor with the same available power. Thermodynamics gives the result for the resistor that the power available at a temperature T in the bandwidth $\Delta\nu$ is

$$P = kT\Delta\nu \tag{9}$$

Substituting equation 9 in equations 7 and 8 we find:

$$T_a = \frac{A_o}{2k} \int B(\theta, \phi) f(\theta, \phi) d\Omega = \frac{A_o}{\lambda^2} \int T_b(\theta, \phi) f(\theta, \phi) d\Omega \qquad (10)$$

where T_a is called the antenna temperature.

If we consider the antenna within a black body of temperature T_o and connected to a resistor whose temperature is also T_o there must be no net power flow between the two, that is, the antenna temperature will equal the resistor temperature:

$$T_o = T_a = \frac{A_o}{\lambda^2} \int T_o f(\theta, \phi) d\Omega \qquad (11)$$

or

$$\frac{\lambda^2}{A_o} = \int f(\theta, \phi) d\Omega \qquad (12)$$

Combining with equation 10 we get:

$$T_a = \frac{\lambda^2}{2k} \frac{\int B_\nu(\theta, \phi) f(\theta, \phi) d\Omega}{\int f(\theta, \phi) d\Omega} = \frac{\int T_b(\theta, \phi) f(\theta, \phi) d\Omega}{\int f(\theta, \phi) d\Omega} \qquad (13)$$

We see from the previous arguments that a lossless antenna is completely specified by the function $f(\theta, \phi)$ at a given frequency. An ideal radio telescope would have $f(\theta, \phi) \sim 1$ inside a small cone $\theta < \frac{g}{2}$ and zero for $\theta > \frac{g}{2}$. If the diameter of the cone is small, the angular resolution will be good, and in addition, equation 13 tells us that the sensitivity to brightness within the cone of acceptance will be high, but equation 13 also shows that the antenna temperature will always be just the average temperature in the beam weighted by $f(\theta, \phi)$.

To make measurements with this idealized antenna we can use an idealized receiver whose output is calibrated in terms of the temperature of a resistor at the input, i. e. in terms of antenna temperature. If we direct this idealized radio telescope at a source whose diameter is larger than g, equation 13 tells us that the output will be directly in terms of the brightness temperature. For a source whose diameter is less than g, we can get the flux by combining equation 3 with equation 13:

$$T_a = \frac{\frac{\lambda^2}{2k} S}{\int f(\theta, \phi) d\Omega}$$

or

$$S = \frac{2kT_a}{\lambda^2} \int f(\theta, \phi) d\Omega \qquad (14)$$

To complete the calibration for flux we must measure $f(\theta, \phi)$ by using a source whose diameter is sufficiently smaller than g. The intensity of this source need not be known, as f is only a ratio. Furthermore, since f is zero for $\theta > \frac{g}{2}$, f may be measured by turning the antenna to completely cover only the solid angle πg^2 on a grid whose mesh is the same order of size as the size over which f changes appreciably $(\sim \frac{g}{2})$.

A real radio telescope will not be as easy to deal with as the ideal radio telescope we have considered. All real radio telescopes have a certain amount of resistive loss. This loss does not affect the previous formulation, as it can be considered as occurring in an

attenuating pad between the antenna and receiver. If the fractional loss is L, the receiver will see a temperature

$$T = (1 - L)T_a + LT_o \tag{15}$$

where T_o is the physical temperature of the antenna and T_a is given by the previous expression. Since L is usually small, its effect on antenna operation is small, but it is difficult to measure or calculate.

A much more important difficulty with real antennas is that f is non-zero over most of the sphere. This means that to determine the antenna characteristics properly we must have a source of plane waves which can be oriented at all angles with respect to the antenna, and measurements must be made at all points on a grid of mesh smaller than the angular size of the fluctuations in f. For an antenna of the sort used in this thesis (beamwidth $0^{\circ}.8$), f can be determined by a measurement at about 1000 directions over the sphere. Loss must also be measured, so the source of plane waves used for the measurement must be of known intensity. Since most large radio telescopes have limited mobility, the source must be movable. Also, the source must be distinguishable from radiation from other sources.

The difficulties involved in such a calibration procedure make it impractical for a large radio telescope. Even if one had the time and patience to carry the procedure through, the errors would probably be great enough to render the results useless. We will therefore consider a practical method of calibrating a radio telescope. The re-

ceiver need only have its output calibrated in units proportional to power. The receiver output for zero input need not be known. Thus, if R is the receiver response, ΔP and ΔT_a are changes in the antenna power and temperature, then $R \propto \Delta P \propto \Delta T_a$. We can absorb any resistive loss in the antenna in the unknown receiver calibration. The only restriction we will need to put on the antenna is that outside some cone $\theta < 3g$, f is small enough that the effect of a strong discrete source moving from a position at which f has a local maximum to one at which f has a local minimum will be negligible compared to the effect of a desired source in the vicinity of $\theta = 0$. This condition will be fulfilled in most radio telescopes where the distant side lobes will be less than 10^{-4}.

We will need at least one source of known intensity with a diameter much less than g located in a region of low or constant background radiation. Let the flux density of the source be S_o and the maximum change in receiver output due to the source be R_o. Then for any other small diameter source with response R_1 the flux will be given by:

$$S_1 = \frac{R_1}{R_o} S_o \tag{16}$$

Using the calibration source we can measure $f(0,\phi)$ for $0 < 3g$. This will require measuring only 49 points and will be easy to carry out.

Now if we measure a spread source whose brightness is given by $B_1(\theta, \phi)$ we see by comparing equations 6 and 7 that we must replace S_1 of equation 16 with $\int_{\theta < 3g} B(\theta, \phi) f(\theta, \phi) d\Omega$. (We can cut the

integral off at $\theta = 3g$ because the contribution of any one source will be negligible outside this cone, unless it covers an appreciable fraction of the sphere.) The result for the distributed source is:

$$\int_{\theta<3g} B(\theta,\phi)f(\theta,\phi)d\Omega = \frac{R_1}{R_o} S_o \tag{17}$$

Using equation 5, we can express equation 17 in terms of brightness temperature:

$$\int_{\theta<3g} T(\theta,\phi)f(\theta,\phi)d\Omega = \frac{\lambda^2}{2k} S_o \frac{R_1}{R_o} \tag{18}$$

If $T(\theta,\phi)$ is essentially constant over the region where $f(\theta,\phi)$ is large enough to make a significant contribution,

$$T_f = \frac{\lambda^2}{2k} \frac{S_o}{\int_{\theta<3g} f(\theta,\phi)d\Omega} \frac{R_1}{R_o} \tag{19}$$

Following Seeger, Westerhout, and van de Hulst (4), we will call this temperature the full beam temperature, and that part of the antenna response within $\theta < 3g$, the full beam. It should be emphasized that the R's in the above equations are changes in the receiver response due to the source in question. In a strict sense we cannot measure this quantity. To do so we would have to turn the source off and measure the response from other sources of radiation, and then turn the source back on and measure the difference. In practice this presents little difficulty because the response due to the other sources changes only slowly with antenna position. Therefore, a sweep of the source

through the antenna beam along some line ϕ = constant will give the necessary information. If we plot the receiver output versus θ during such a sweep, the result will be something like figure 1.

R_1 can be measured as shown in figure 1. If as is indicated in the figure the width of the response at half response (g_1) is about equal to the half width of the response to a point source, the source diameter must be much less than g and we may obtain the flux density from equation 16. If, however, the width g_1 is much greater than g, we can obtain the brightness temperature from equation 19.

In the intermediate case, where g_1 is between these limits, the problem is not as simple. Measurement of the flux density requires a measurement of the complete response of the full beam to the source. This will require measurement of the response at a grid of points of mesh g/2 over a solid angle (c) sufficient to cover any overlap of the source and the full beam.

In order to carry out the subsequent calculations it will be necessary to introduce a coordinate system in the celestial sphere. Although the present argument does not require specifying the type of coordinates used, it will be helpful later to introduce a system which reduces to a rectangular system (x, y) in the vicinity of the source with the point (0, 0) on the centroid of the source. Let x increase toward the east along a circle of constant declination and y increase to the north along a circle of constant hour angle. x and y are measured in radians. It will be convenient to introduce a similar system in the antenna centered system. Call this system (ξ, η),

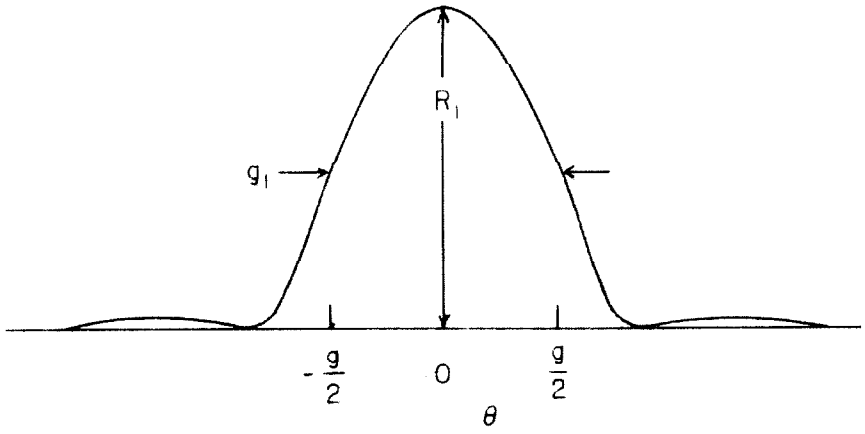

Figure 1. Receiver output during a sweep across a source.

and let the point $(0, 0)$ coincide with $\theta = 0$ and the positive ξ axis be parallel to the positive x axis. Let the direction $(0, 0)$ in the antenna system have coordinates (x_o, y_o) in the celestial system and the source brightness distribution be $B(x, y)$ in the celestial system. In the antenna system the brightness distribution will be $B(\xi+x_o, \eta+y_o)$. We may now rewrite equation 17 as:

$$\frac{R_1}{R_o} S_o = \int_{(\xi^2+\eta^2)^{1/2}<3g} B(\xi+x_o, \eta+y_o) f(\xi, \eta) d\Omega \qquad (20)$$

(We will retain $d\Omega$ as the differential of solid angle in the antenna system and introduce $d\omega$ as the differential of solid angle in the celestial system.)

Now that the details of coordinate systems are straight, we can return to the problem of finding the flux density from an extended source. The technique is to integrate the response (R_1) over antenna positions around the source, that is, form the integral:

$$\frac{S_o}{R_o} \int_c R_1 d\omega = \int_c d\omega \int_{(\xi^2+\eta^2)^{1/2}<3g} d\Omega B(\xi+x_o, \eta+y_o) f(\xi, \eta) \qquad (21)$$

The function B represents a physical quantity and therefore will be continuous, bounded, etc., and we can interchange the order of integration. We have chosen the area c, so that for $(\xi^2+\eta^2)^{1/2} < 3g$, $B(\xi+x_o, \eta+y_o)$ will be zero for (x_o, y_o) on or outside the boundary of c. Therefore integrating over x_o, y_o will cover all non-zero values

of B and the integral $\int_C d\omega_o B(\xi+x_o, \eta+y_o)$ will be independent of ξ and η. Using equation 3, we have the result:

$$\int_C d\omega_o B(\xi+x_o, \eta+y_o) = \int_C d\omega_o B(x_o, y_o) = S \tag{22}$$

Combining equations 21 and 22 we get

$$S = \frac{S_o}{R_o} \frac{\int_C R_1 d\omega_o}{\int_{\theta<3g} f(\theta,\phi)d\Omega} \tag{23}$$

We now have the flux of the source in terms of easily measurable quantities.

In many cases an error of a few percent will be acceptable, and the integrals in equation 23 need only be carried out over the central lobe or main beam of the antenna response. This will reduce the work involved considerably.

We will now find the quantities needed to apply equations 16, 19, and 23 to source measurements with the antenna used in the survey of the galactic plane to be described in the next section. The required quantities are: S_o/R_o and $\int_{\theta<3g} f(\theta, \phi)d\Omega$. S_o/R_o depends on the receiver as well as the antenna, and is therefore likely to change with time. It was measured every night and calibrations made as a function of time. In terms of the contour intervals used in the maps, the source Virgo A gives a response of about 24 units. We will derive the flux of this source in Section 3 from measurements at other observatories. The result is $\sim 300 \times 10^{-26}$ $Wm^{-2}(c/s)^{-1}$. The ratio

S_o/R_o is therefore 12.5×10^{-26} $Wm^{-2}(c/s)^{-1}$ per unit.

Figure 2 gives a contour map of the antenna pattern determined from sweeps of the antenna in the region surrounding the sources Cas A and Cyg A. These sources have diameters of 3.'5 and 1.'7 and may be considered as point sources. There is some background radiation around both of these sources, but it appears at different positions for the two, so that by combining the two observations properly the true antenna pattern can be found. The function which is plotted is actually $f(\theta,\phi+\pi)$, since we have plotted the response versus antenna direction. Integrating the contours of figure 2 with a planimeter we obtain the result that:

$$\int_{\theta<3g} f(\theta,\phi)d\Omega = 0.789 \text{ sq. degree} = 2.40 \times 10^{-4} \text{ sterradian} \quad (24)$$

Five percent of this is contributed by the two declination side lobes. Putting in all of the numbers we can rewrite equations 16, 19, and 23 as

$$S_1 = 12.5 \times 10^{-26} R_1 \ (Wm^{-2}(c/s)^{-1}) \quad (25)$$

$$T_f = 1.85 \ R_1 \ (^oK) \quad (26)$$

$$S_1 = 12.5 \times 10^{-26} \ \frac{\int_c R_1 d\omega_o}{0.789}$$

In addition to the flux of a source, it would be useful to derive information about the brightness distribution. If the beamwidth of the antenna is sufficiently small compared to the size of the structure of

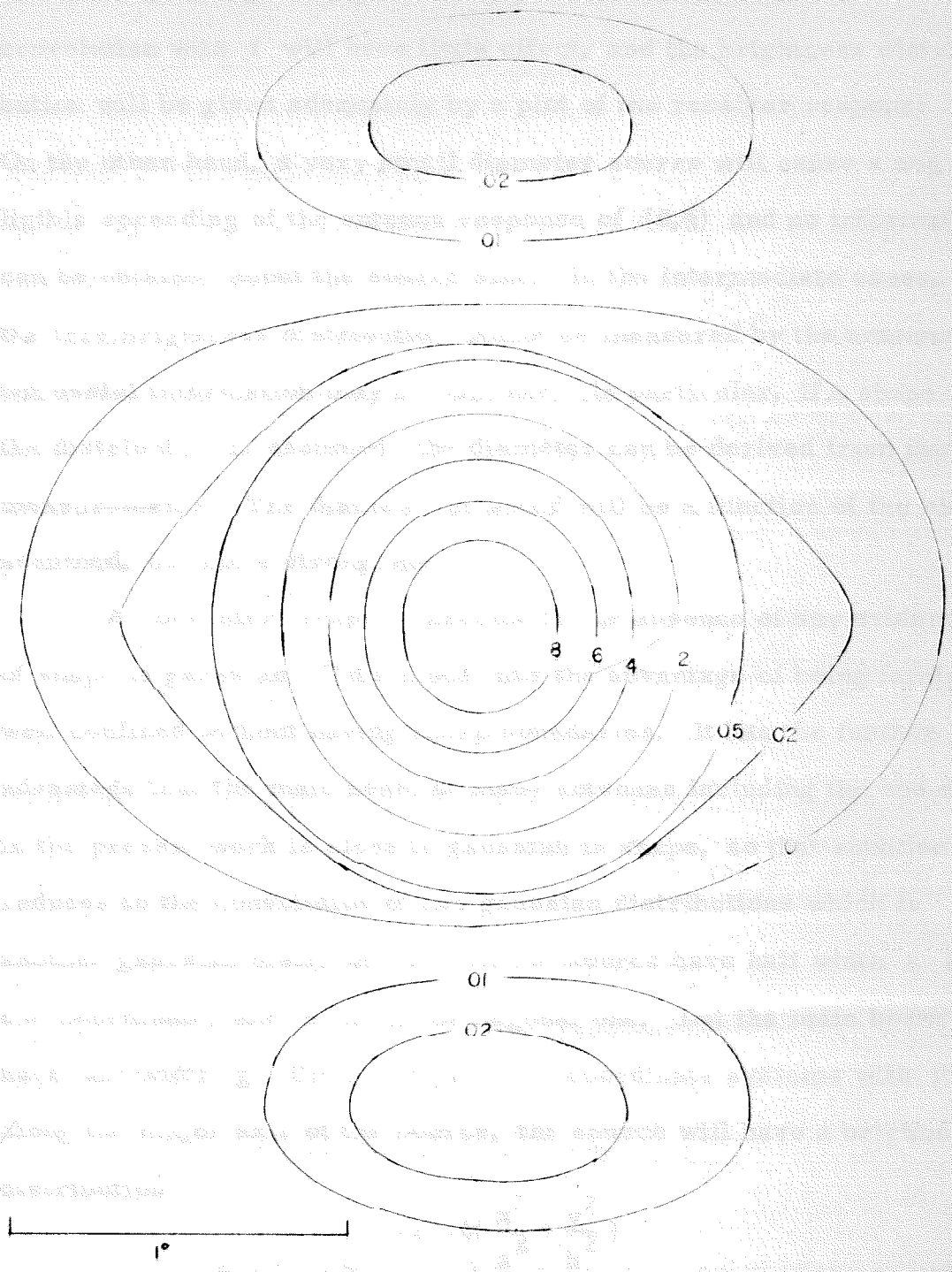

Figure 2. Antenna pattern of the antenna used in this work.

the source, the spreading of the brightness distribution due to the convolution with f will have little effect, and the brightness distribution will be given adequately by a plot of the receiver response R. On the other hand, a very small diameter source will cause a negligible spreading of the antenna response of (θ,ϕ) and no information can be obtained about the source size. In the intermediate cases, the true brightness distribution cannot be measured by the antenna, but useful information may be obtained. In particular, if a shape for the distribution is assumed, the diameter can be derived from the measurements. The diameter obtained will be a function of the shape assumed, but not a strong one.

A convenient shape to assume in the absence of any evidence of shape is gaussian. This model has the advantage of being fairly well confined without having sharp boundaries. It has the further advantage that the main beam of many antennas including the one used in the present work is close to gaussian in shape, so that equation 20 reduces to the convolution of two gaussian distributions which is another gaussian distribution. Let the source have half width a in one coordinate, and b in the orthogonal one. Let the main beam have half width g. Using the previous coordinate systems with x along the major axis of the source, the source will have a brightness distribution:

$$B(x, y) = B_o e^{-2.76\left(\frac{x^2}{a^2} + \frac{y^2}{b^2}\right)} \tag{28}$$

and the beam will have a shape:

$$f(\xi, \eta) = e^{-2.76\left(\frac{\xi^2+\eta^2}{g^2}\right)} \tag{29}$$

The flux of the source will be

$$S = \int_{-\infty}^{\infty} dx \int_{-\infty}^{\infty} dy\, B_o e^{-2.76\left(\frac{x^2}{a^2} + \frac{y^2}{b^2}\right)} = 1.14\, B_o ab \tag{30}$$

(We will restrict ourselves to sources that are small enough for the rectangular coordinate systems to be valid approximations wherever the exponentials are significantly greater than zero.) The response of the antenna to the source (equation 20) will be:

$$R\frac{S_o}{R_o} = B_o \int_{-\infty}^{\infty} dx \int_{-\infty}^{\infty} dy\, e^{-2.76\left[\frac{(\xi+x_o)^2}{a^2} + \frac{(\eta+y_o)^2}{b^2} + \frac{\xi^2}{g^2} + \frac{\eta^2}{g^2}\right]} \tag{31}$$

Rearranging terms and carrying out the integral this becomes:

$$R\frac{S_o}{R_o} = 1.14\, B_o ab \frac{g^2}{[(a^2+g^2)(b^2+g^2)]^{1/2}} e^{-2.76\left(\frac{x_o^2}{a^2+g^2} + \frac{y_o}{b^2+g^2}\right)} \tag{32}$$

Letting $W_1^2 = a^2 + g^2$ and $W_2^2 = b^2+g^2$ and substituting from equation 30, equation 32 becomes

$$R\frac{S_o}{R_o} = S\frac{g^2}{W_1 W_2} e^{-2.76\left(\frac{x_o^2}{W_1^2} + \frac{y_o^2}{W_2^2}\right)} \tag{33}$$

Thus, if we measure the half width of the receiver response along the major and minor axes, we can get the diameters of the source from:

$$a \approx (W_1^2 - g^2)^{1/2}$$
$$b \approx (W_2^2 - g^2)^{1/2} \qquad (34)$$

If we measure the peak response (R_p) to the source ($x_o = y_o = 0$) we can get the flux density from:

$$S = \frac{S_o}{R_o} R_r \frac{W_1 W_2}{g^2} \qquad (35)$$

III. THE RECEIVER

In the foregoing section we have mentioned the function which a receiver is required to perform--select a frequency response band, and produce a high level output which changes in proportion to changes in the input power within the response band. Undesirable properties of a receiver are the noise power added by the receiver to the input power, changes in output level resulting from internal changes in the receiver, changes in the proportionality constant between output and input (gain) with time, and lack of a linear relation between input power and output.

A block diagram of the receiver used in the present work appears in figure 3. It is seen to be a switched radiometer of the sort described by Dicke (5). The mixer is a double sideband mixer, so that two bands are received at the local oscillator frequency plus and minus the i. f. frequencies. During the early part of the observations the i. f. center frequency was 30 Mc/s. Later this was changed to 10 Mc/s. In both cases the bandwidth was about 7 Mc/s. The diode switch and the mixer-preamp chassis were mounted in a box behind the focus. The remainder of the receiver was mounted in the room at the base of the antenna.

The operation of the diode switch is based on the fact that the diodes present a low impedance across their terminals when forward biased, and a high impedance when back biased. The configuration of the diode switch is shown in figure 4. The construction is with

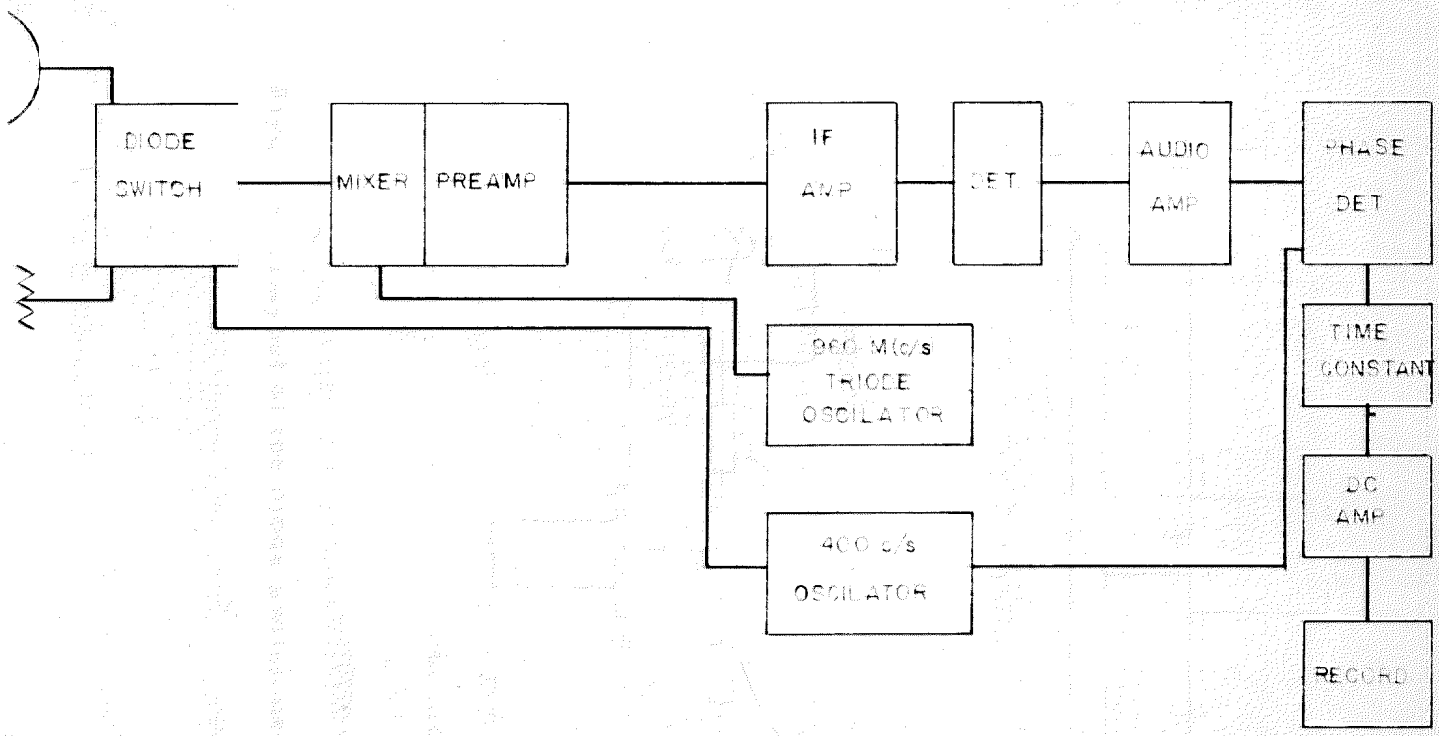

Figure 3. Block diagram of the receiver.

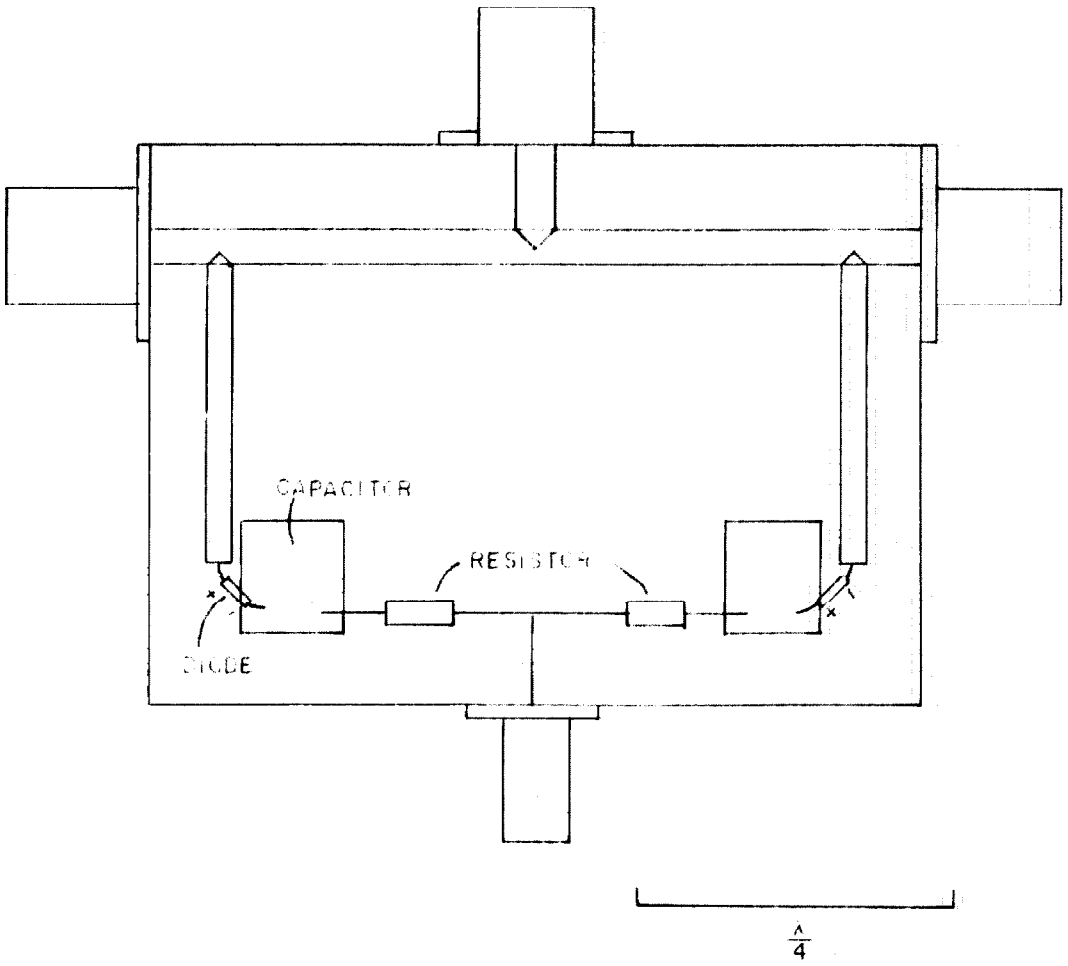

Figure 4. Layout of the diode switch used in the receiver.

brass rods suspended by the connectors above a brass plate. The small diameter rods connecting the gold bonded germanium diodes to the main "T" have an impedance of about 100Ω and serve to match the diode impedance to that of the line for reduced forward loss. The diodes are connected to bypass capacitors constructed of a brass sheet insulated by sheet mica. The switching rate is 400 cps and the switch is fed by a 400 cps square wave of about 10 V amplitude. Over the required bandwidth the isolation is greater than 20 db and the forward loss $\lesssim$ 0.5 db.

The diode switch switches the mixer input between the antenna feed horn and a resistor which is kept in a thermos bottle of liquid nitrogen boiling at atmospheric pressure (~77°K). The resistor is a platinum film deposited on a ceramic core mounted as the inside conductor of a shorted coax with tapering outer conductor. The unit is basically the 50Ω termination manufactured by Stoddard Aircraft Radio Co. The resistance unit, however, was selected from a special run of high resistance units (about 60Ω) to have a resistance of 50Ω in liquid nitrogen.

The mixer was mounted on the preamp chassis. The crystal (a 1N21E) was matched for lowest noise to the 50Ω output impedance of the switch with a quarter wave transformer, and to the first stage of the preamp with a T section transformer. The first stage was a cascode consisting of a Western Electric 437 and a Western Electric 417.

The noise added by the mixer-preamp combination was equi-

valent to adding about 300°K to the input temperature with the 30 Mc/s i. f. center frequency and about 200°K with the 10 Mc/s i. f. frequency. The switch and connecting cables added another 100°K to bring the total system temperatures to 400°K and 300°K.

The output of the i. f. amplifier was rectified and fed to an audio amplifier tuned to 400 cps which drove a transistor switch phase detector. The phase detector output was fed through a one-second time constant DC amplifier to a Leeds and Northrup potentiometer-type recorder.

The detector was used in a range in which the change in output voltage was almost linearly proportional to the change in i. f. output voltage, i. e. proportional to the change in the square root of i. f. power. In the normal operation of the receiver, the local oscillator frequency could be adjusted to a frequency near 960 Mc/s, so that with the antenna pointed at the cold sky, the output power was the same whether the receiver was switched to the antenna or the nitrogen cooled resistor. The exact balance was probably brought about by a small mismatch in the pick-up horn of the antenna. While adjusted for balance in this way, there will on the average be no component in the output of the detector at the switching phase, and the output of the phase detector will average to zero. The output power under these conditions will be proportional to the system temperature (T_r). If we turn the antenna onto a source which raises the antenna temperature by an amount T_1, the output of the detector will now contain a square wave whose amplitude is proportional to $(T_r + T_1)^{1/2} - (T_r)^{1/2}$

which is in phase with the switching voltage. The response of the recorder will be in proportion to this same quantity. If $T_1 \ll T_r$ we may usefully expand this quantity in a power series:

$$R_1 \alpha (T_r+T_1)^{1/2} - (T_r)^{1/2}$$
$$\approx (T_r)^{1/2}\left[\frac{1}{2} \frac{T_1}{T_r} - \frac{1}{8}\left(\frac{T_1}{T_r} \right)^2 + \frac{1}{16}\left(\frac{T_1}{T_r} \right)^2 - \dots \right]$$

or

$$R_1 \alpha T_1\left[1 - \frac{1}{4} \frac{T_1}{T_r} + \frac{1}{8}\left(\frac{T_1}{T_r}\right)^2 - \dots \right] \qquad (36)$$

Excluding the sources Cas A and Cyg A which were treated separately, the maximum deflection observed on the survey was the 80 unit deflection on the peak of Sgr A. At the time that region was done the receiver temperature corresponded to about 320 units. The departure of the receiver from linearity was therefore about 6% at Sgr A. At the level of the calibration source Vir A, the nonlinearity amounted to about 2%. Except for the peak at M 17, the remaining contours are therefore in error by less than 2%. The sources Cas A, Cyg A, Sgr A and M 17 are corrected in the list for receiver non-linearity, but the effect was otherwise disregarded.

IV. FLUX DENSITY OF THE STANDARD SOURCES

In the first part, while discussing the calibration of antennas, we assumed that there is at least one strong point source in the sky whose flux density is known at the frequency in question. It is at this point that we encounter one of the most difficult problems in radio astronomy--the determination of absolute flux densities. The problems that caused us to give up independent calibration of the antenna will, of course, affect every other radio telescope. There are two solutions to the problem. Construct an antenna which is sufficiently simple that its response can be calculated, and the construction carried out to a sufficient degree of accuracy, or find a source whose flux density is known from physical arguments.

In the latter category two sources have been used--the moon and forests. The temperature of the moon is not accurately known as yet, and is a function of frequency. The "pinewood" calibrations as carried out by Muller and Westerhout [cf. (6)] differ by about 20% from Mezger's results (7) using a nearby wood. Mezger's method would appear to be more nearly correct and his results agree well with other observations.

All other methods use an antenna whose response can be calculated. This antenna is used to transmit a signal of known flux for calibrating another antenna, to measure the flux of a strong source directly, or to substitute for a larger antenna in a comparison calibration of the large antenna.

In any of the absolute flux measurements, the receiver response

must be known in terms of antenna temperature to better than the desired accuracy of the measurement. This entails problems of accurately matching the antenna to the receiver, and obtaining an accurately known noise source. The problems of absolute flux measurements are sufficiently great and different from those of other observations, that such measurements are usually carried out as an independent program.

At Caltech no program of absolute flux measurements has been carried out. We must therefore rely on measurements made at other observatories. These measurements are at different frequencies from the one used in the present work, so that we must interpolate to find the flux at our frequency. For this end the literature was searched for absolute flux measurements. References (7) to (30) are to papers in which absolute flux measurements have been reported. Figures (5) through (8) in Appendix I are plots of these measurements for the four sources Cas A, Cyg A, Tau A, and Vir A. Table I in Appendix II explains the abbreviations used in figures 5 through 8. The straight line in each of these figures is what was considered the best straight line fit to the data. These lines reflect a subjective weighting of the points on the basis of an evaluation of the experiments. In the case of Vir A, which was not measured by several of the authors the line was drawn taking into account the fact that intensity ratios are measured more accurately than absolute intensities. The Vir A results of several of the authors were therefore mentally changed by the factor necessary to bring their Cas A values on the median Cas A line.

From figure 8 we read the flux of Vir A at 960 Mc/s to be 280×10^{-26} $W/m^{-2}(cps)^{-1}$. This is sufficiently close to the value of 300×10^{-26} which has been used previously at Caltech, that the previous value is retained in subsequent parts.

V. OBSERVATIONS

A survey was made of the 960 Mc/s radiation within 10° of that part of the galactic plane visible from the Owens Valley Radio Observatory.

The antenna used in these measurements was one of the observatory's two 90-foot steerable paraboloids. These antennas are mounted equatorially, and are driven by two-phase servo motors in both coordinates. In declination the available drive rates are $\pm 1^{\circ}$/minute, or $\pm \frac{1}{4}^{\circ}$/minute, depending on the rate motor installed. In right ascension, the rates are $\pm 1^{\circ}$/minute or zero $\pm$ siderial rate or zero. The slew rate is 8°/minute in either coordinate. The sky coverage of the antennas is $+ 90^{\circ}$ to $- 50^{\circ}$ in declination, and ± 4 hours in hour angle for $\delta > -25^{\circ}$. For $\delta < -25^{\circ}$ the hour angle limits are reduced by the mount design, but not as much as the reduction by the mountains on the west.

Observations were made three ways. In an α-drive, the antenna was set at the desired declination and the earliest desired right ascension. It was then driven toward a later right ascension at 1°/minute. About half of the survey was made with this type of observation. Since for $\delta < -40^{\circ}$ the changing ground radiation in the back and side lobes of the antenna was larger when the antenna was moved, observations were made with the antenna stationary in this region. The celestial motion is thus at the siderial rate of about $\frac{1}{4}^{\circ}$/minute for α-drifts. For $\delta > +40^{\circ}$, a shorter traverse of the galactic plane can be made with motion in declination. In this region δ-scans were

made with the antenna tracking a given right ascension and driven north at a rate of 1^{o}/minute. All of these rates are small enough that the 1 sec time constant of the receiver could be ignored in the reduction of the data. At the end of a scan, the antenna was set to the next declination (or right ascension) and slewed back to the starting point. The resulting high-speed scan provided a rough check on the slow scan to follow. A sample scan is shown in figure 9. The spacing of successive observations in right ascension or declination was determined by the complexity of the regions involved. Table 2 gives the method of observation and spacings used for the various sections of the survey.

The length of the scans also depended on the region being observed. At least every 5^{o} a scan was extended sufficiently on either side that the level was constant for several degrees. Records in between these long scans were often made somewhat shorter to save time.

For the greater part of the survey the observations were carried out at hour angles of less than two hours. This reduces the change in the amount of ground radiation picked up by the antenna during a scan. All observations were made between sunset and sunrise to avoid the effects of solar radiation in the side lobes.

Each night an observation was made of the source Vir A, or if that source was not available, Cas A or Cyg A was substituted. The ratio of these sources, uncorrected for detector law was taken from the observations of Harris and Roberts (31), using the same system. The value observed for Cas A or Cyg A were converted to

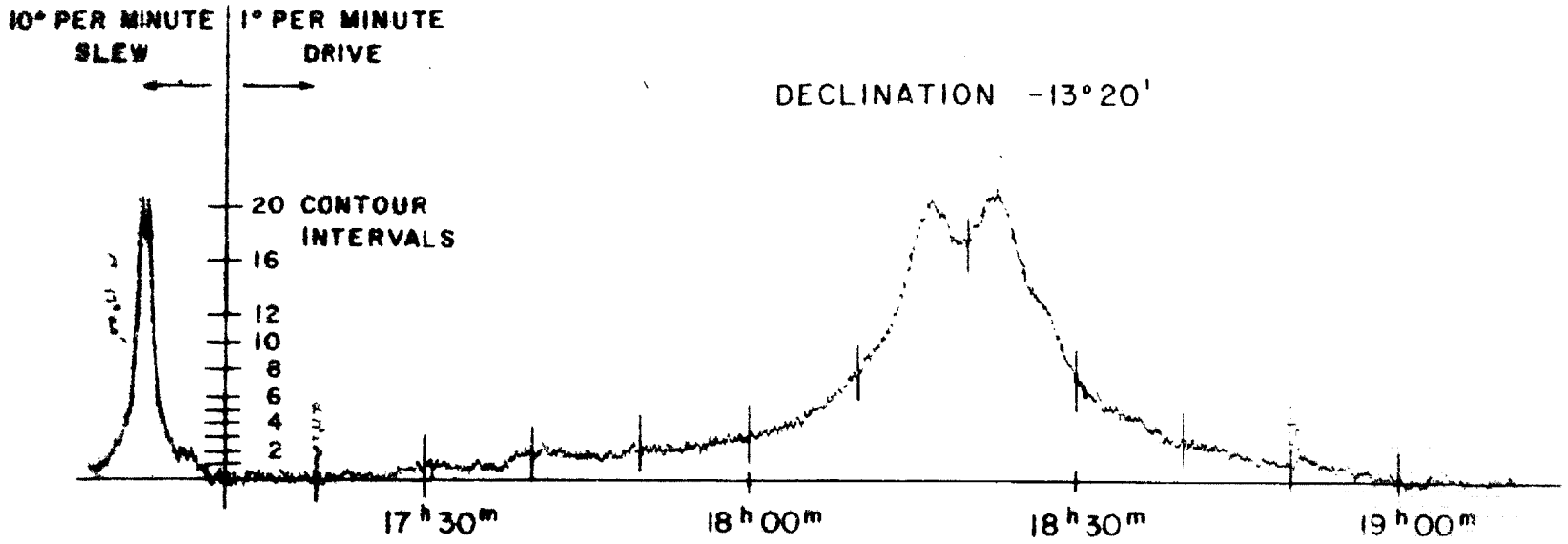

Figure 3. Sample record of an observation at δ = -13° 20' showing the slew at the beginning and the baseline drawn in through the end portion of the record

Table 2. Type and spacing of observations

Figure	Region	Type of Observation	Average Spacing of Observations
2	16^h00^m to 18^h20^m -48° to -30°	α drift below -40° α drive above -40°	$0^\circ.5$
3	17^h00^m to 19^h40^m -30° to 0°	α drive	$0^\circ.6$
4	18^h00^m to 21^h00^m 0° to $+30^\circ$	α drive	$0^\circ.5$ from 0° to $+20^\circ$ $1^\circ.0$ from $+20^\circ$ to $+30^\circ$
5	18^h30^m to 21^h15^m $+30^\circ$ to $+60^\circ$	α drive	$0^\circ.7$
6	21^h00^m to 1^h00^m $+40^\circ$ to $+70^\circ$	δ drive	7^m
7	1^h00^m to 5^h00^m $+40^\circ$ to $+70^\circ$	δ drive	7^m
8a	4^h30^m to 7^h00^m 0° to $+40^\circ$	α drive	$1^\circ.5$
8b	6^h00^m to 8^h00^m -40° to 0°	α drive	$1^\circ.5$
9	8^h00^m to 9^h30^m -48° to -40°	α drift	$0^\circ.5$

equivalent observations of Vir A using these ratios so that Vir A remains as the flux calibration standard for the survey, even though it was not available for night-time observation during part of the survey. The night to night values observed for Vir A showed a scatter of a few percent. The mean over several days, however, was a much more constant quantity. The data has been reduced using an average calibration for each of the separate observing periods in the expectation that the receiver constants were probably almost constant, and the night to night fluctuations were due to noise or some other short term effect.

VI. REDUCTION OF DATA

A zero line was drawn on each record above which intensity changes were measured. On the long records this line was drawn between the flat parts at either end. A sample of such a record with its zero line drawn in is shown in figure 9. The zero lines on the shorter records were drawn in on a light table with the aid of the adjacent longer records. After the zero line was drawn, a series of lines was drawn on the record parallel to it at distances above it corresponding to the adopted contour intervals. (The intervals are integral multiples of the "units" of part I.) The right ascension or declination corresponding to the intersection of contour parallels and the record were read off and plotted on equal area, celestial coordinate charts of scale 2 cm = 1 degree. Contours were drawn through these points and the outer contours were smoothed somewhat. The coordinate grids were then redrawn to simultaneously correct for the antenna pointing errors as observed by Harris and Roberts (31), process the maps to the standard epoch 1950.0, and correct for refraction where it was greater than 2'. The large scale maps were photographically reduced and redrawn for publication. Figures 10 to 17 in Appendix I are reproductions of these maps on a new galactic coordinate grid (32). Equations 25, 26, and 27 give the calibration of the contour intervals on these maps in terms of point source flux density, full beam temperature, and extended source flux density.

Table 3 in Appendix II is a list of the 112 discrete sources found on the maps. The first column is the serial number of the source from

the CTB list (33). Column two gives previous radio designations for the source, or in the case of well known sources, the common or optical name. The previous radio designations for this column were taken from the lists of:

K	Kuzmin et al.	3125 Mc/s	(34)
UoB	Müller	1420 Mc/s	(26)
W	Westerhout	1390 Mc/s	(22)
HB	Hanbury Brown and Hazzard	185 Mc/s	(13)
3C	Edge, Shakeshaft et al.	159 Mc/s	(35)
M	Mills, Slee and Hill	85.5 Mc/s	(36)
R	Rishbeth	85.5 Mc/s and 23 Mc/s	(37)

Column three gives the right ascension of the source for epoch 1950 as read either from the chart, or from the original records. Column 4 is the ten-year precession for the right ascension (38). In a similar way columns 5 and 6 are the declination and declination precession. In columns 3 and 5 a number has been included in parenthesis after the source position to indicate an estimated probable error in the positions. The meanings of the numbers are given in Table 4 in Appendix II.

Column 7 gives the peak response of the receiver to the source above the background level. It is equal to the factor $R_1(S_o/R_o)$ found in equations 17, 18, and 19. In the case of a point source this peak response is equal to the flux density of the source in units of 10^{-26} $Wm^{-2}(cps)^{-1}$.

Column 8 gives the flux density of the source in units of $10^{-26} W m^{-2} (cps)^{-1}$. For most sources the flux density in column 7 is taken from the peak response of the receiver using equation 35 (gaussian model). W_1 and W_2 for this equation are obtained from the source diameter as listed in column 9 or 10 using equation 34. The half power width of the antenna beam (g) is taken from figure 2 to be $0.^{\circ}8$. The flux density of several sources which were sufficiently separate from the background was obtained from equation 27 using a planimeter integration of the contours.

In column 9 a diameter (or pair of diameters) of the source is listed. These were obtained from the half widths of the contours (W_1 and W_2) using equation 34 (gaussian model). For many sources a more accurate diameter was obtained from the original records than from the contours. In many other cases the source diameter was sufficiently small that a more accurate diameter was obtained in the interferometer observations which will be described later. In these cases the diameter is given in column 10.

VII. OPTICAL IDENTIFICATIONS

The positions of the 112 sources in table 3, along with the positions of three or more nearby stars taken from the AGK_2 (39) or Boss (40) catalogs, were plotted on vellum to the scale of the Palomar sky survey using coordinate charts prepared by Herzog. These vellum overlays were then lined up on survey prints, and the area of the source was searched for an optical identification. Comments on identifications or interesting aspects of the optical field are given in the notes to table 3 (in Appendix II). The southern limit of the Palomar survey is -39°. For declinations below that limit, prints of a series of plates taken by Matthews with the 48" Schmidt camera were used. In the notes, emission nebulae are referred to by number in the Sharpless (41) catalog for declinations greater than -39° and the Mt. Stromlo catalog of Gum (42) otherwise. In several cases NGC or IC numbers have been retained.

VIII. SPECTRA OF SOURCES

Some idea of the nature of a radio source can be obtained from its spectrum. Table 5 in Appendix II presents spectral information on the 112 sources listed in table 3. It lists the flux density of each of the 67 sources which have been previously observed at each of the frequencies at which it has been observed. The flux densities in this table were taken from the same catalogs used for the "previous radio designation" column except for 1420 Mc/s. At this frequency, the observations of Müller (26) do not contain flux densities for the sources. The observations of Lynds (43) at 1420 Mc/s of several HII regions have been added, however.

The flux densities quoted by Westerhout at 1390 Mc/s have been multiplied by a factor of 25/31 in table 5. This compensates for the difference between the "pine wood" flux density of Cas A at 1390 Mc/s and the value read from figure 5. Similarly, Mills' 85.5 Mc/s flux densities have been multiplied by 20/24 to change his value of Vir A to agree with figure 8. These changes reduce all of the measurements to a common calibration, and accomplish much the same thing that Harris and Roberts (31) did by computing relative spectral indices.

The flux densities for each of the sources were plotted against frequency on log-log coordinates in the same manner as figures 5-8. On the usual assumption that the flux density of a source is proportional to ν^{x}, the points from a source should lie on a line whose slope is the spectral index (x) in this plot. The spectral indices given in column 11 of table 3 were read from these graphs using an overlay containing

lines of various slopes. In the case of sources which were observed at more than two frequencies, a scatter is given along with the spectral index. This scatter gives the maximum and minimum slope for a line which can be drawn reasonably through the points. It does not contain the uncertainty in the points. This uncertainty can have a large effect, especially where observations are available over only a narrow frequency range. The errors in flux density for most of the sources in table 5 come not so much from errors in calibrating the radio telescope, as from errors in the size corrections and background radiation level. A few of the sources listed in table 5 do not have spectral indices in table 3 because the values obtained were unreasonable.

IX. INTERFEROMETER OBSERVATIONS

Several of the discrete sources found on the survey have diameters sufficiently smaller than the main beam of the 90' antenna at 960 Mc/s that only an upper limit could be placed on this diameter from measurement with the single antenna. In order to measure the diameters of these sources, a series of observations were made using the Caltech variable spacing interferometer at 960 Mc/s. This interferometer has been described by Read (44). These measurements were made concurrently with the general brightness distribution programs of Moffet (45) with an east-west baseline, and Maltby (46) with a north-south baseline.

Moffet writes the response of an interferometer as:

$$R(t) = \int\int B(x, y) f(x-x_o, y-y_o) \cos \{2\pi [s_x(x-\Omega t)+S_y y] +\Psi\} dx\, dy \quad (37)$$

The symbols used in this expression are the same as those used in the first part except for:

t = local siderial time

Ω = siderial rate

s_x = projection of the baseline on the x-axis at $x = 0$, $y = 0$

s_y = projection of the baseline on the y-axis at (0, 0)

Ψ = instrumental phase error

The baseline of the interferometer (s) is the distance between the vertices of the two paraboloids measured in wavelengths. It has been assumed in equation 37 that the two antennas are identical, and are

pointed at the same position in the sky. If, as is usual, they are pointed toward the centroid of the source, $x_o = y_o = 0$.

It is seen from equation 37 that the response of the interferometer at a given pair of baseline projections s_x and s_y gives one point on the two-dimensional Fourier transform of the brightness distribution of the source. If the response were measured at a sufficient number of values (s_x, s_y), the complete transform and therefore the complete brightness distribution would be known. The present observations are limited to antenna spacings of 195 wavelengths in the east-west direction, or 195, 389, 779, or 1557 wavelengths in the north-south direction. The observations with the north-south configuration were all made with the source near the meridian so that $s_x = 0$, s_y = (antenna spacing) x cos [$\delta - 37^{\circ}13'53.8''$], where δ = the declination of the source, and $37^{\circ}13'53.8''$ is the latitude of the observatory. The east-west observations were made at hour angles to produce one or more of three possible effective spacings. These effective baselines were $s_x = 195$, 169 and 126 wavelengths, and s_y small.

Many of the sources were not observed at all of the possible spacings because of limited observing time available. The rather limited data from these observations have been reduced to the east-west and north-south diameters of column 10 of table 3, quoting the diameter of a gaussian distribution whose transform best fits the observed transform. In several cases the transform was more complex than that of a simple gaussian. In these cases an interpretation has been made in terms of the sum of a broad and a narrow gaussian. The

width of the narrow gaussian is given in the notes to table 3.

The interferometer measurements have complemented the diameter measurements made with the single dish, but the jump from a 90' antenna to a minimum effective spacing of at least 126λ has left a hole in the range of diameters which could be measured on many sources from about $0^{\circ}.5$ down to $0^{\circ}.2$. Several sources have diameters within this range. Several of the small diameter sources were measured more extensively by Moffet (45) or Maltby (46) than in the present work. Their values are quoted in column 10 for these sources.

X. DISCUSSION OF SOURCE LIST

The source list (table 3) lists 112 discrete sources, of which 67 have been observed at other observatories. Of the remaining 45, 13 can be identified with optical objects. Six of the remaining sources are so weak that without further evidence their existance must be doubted. Thirty-one sources have been identified with emission nebulae. Of these 31 sources, the spectra of 18 are indicated in column 11 of table 3. Ten of these have approximately flat spectra ($|x| < 0.2$) corresponding to the expected value for a thin emission nebula. Two of the sources have positive spectral indices which would result from the nebula becoming thick at low frequencies. Two of these sources (numbers 9 and 91a) have $x \sim -1.4$ which implies either an error in the observation, or that the source of radiation is non-thermal, the former being more likely. Thirteen other sources are possibly associated with emission nebulae, with six of these having spectra measured as flat.

Nine sources have previously been identified as supernova remnants. Sources numbers 1 and 26 (28 and 29 are considered to be part of number 26) are probably also supernova remnants. Source number 13 is a large diameter object located in a region containing several long filaments of emission. Bolton has suggested that this source may be a supernova remnant. Sources numbers 34, 37, 45 and 47 have diameters of $1/2^{\circ}$ to 1° and relatively flat spectra, but produce peak temperatures on Mills' survey of above $20,000^{\circ}K$. The large diameter implies that the sources are nearby, so that one would

expect little of the "background" radiation to be in front of the source. The high peak temperatures on Mills' survey therefore lead to high kinetic temperatures for the sources. D. Mathewson (personal communication) has suggested that two of these sources may be located at the edge of the "3 kpc arm," and the high temperatures may be the result of collisional excitation. The same explanation might also apply to the other two sources. Another explanation of these sources (suggested by Mills (47)) is that they may be supernova remnants. Number 37 corresponds closely to the picture of a type II supernova remnant developed by Harris (48) and the others fall close to the curve. They are located in highly obscured regions, so that their nature must be decided on radio observations only.

On the basis of diameter, seven sources are suggested as being possibly extra galactic. This leaves a total of thirty-seven sources which can be expected to exist, but whose physical nature is not suggested by the present data.

XI. THE DISK COMPONENT

The radio radiation from the Galaxy can be conveniently divided into four components: (1) the discrete sources closely concentrated along $b^{II} = 0$, (2) the part very strongly concentrated around the plane, or disk component, (3) the very broadly distributed part, or halo, and (4) the line radiation from neutral hydrogen.

The present work is limited to observations of the first two components. The first part has been discussed in earlier sections. In observing the second component, the effect of the halo on the results is small, because scans were made only across the short distance of the plane with a minimum of motion along the plane. That is, the disk component has been separated from the halo in the same manner that the discrete sources have been separated from the total of the plane and halo.

In investigating the disk component, however, we will want to find out something of the physical conditions in the plane of the Galaxy. The subtraction of the extrapolated halo component from the disk component inherent in the data must be overcome, and the total radiation from the direction of the plane found. After this is accomplished, the spectrum of the radiation can be determined by comparing surveys made at different frequencies. Knowledge of the spectrum will allow the radiation to be separated into two components corresponding to the two processes of generation. Finally, the spacial distribution of these two sources can be approximated with the aid of a model.

In order to find out as much as possible about the spectrum of the radiation from the plane, it would be nice to compare several surveys. There is insufficient knowledge of the sky temperature above 400 Mc/s, however, to derive more than one zero point of temperature for surveys above that frequency. In addition, there is only one survey below 960 Mc/s which has been made with a resolution comparable to that of the present work. We will therefore compare the present work with that of Hill, Slee and Mills at 85.5 Mc/s (49) to determine the spectrum.

Figures 18 through 22 show cross sections through both of the surveys at several galactic longitudes which were found to be free of discrete sources on both surveys. In contrast to the present work, the 85.5 Mc/s survey is a measurement of the total temperature. For the data in table 6, a zero level for the 960 Mc/s survey has been determined from a 400 Mc/s map of the part of the sky with $\delta > -30^{\circ}$ made by Seeger et al. (49). A separate zero level was determined for each of the cross sections by reading the temperature on the 400 Mc/s map at the end points. The average of these two temperatures was changed to a 960 Mc/s temperature using a temperature spectral index of 2.50. The number to use for this spectral index is not known, but the result is not strongly dependent on the number used because the frequency range is small.

The first two columns of table 6 list various positions on the cross sections of figures 18-22 and three other positions on the equator. Column 3 of this table gives the total temperature at 85.5 Mc/s for

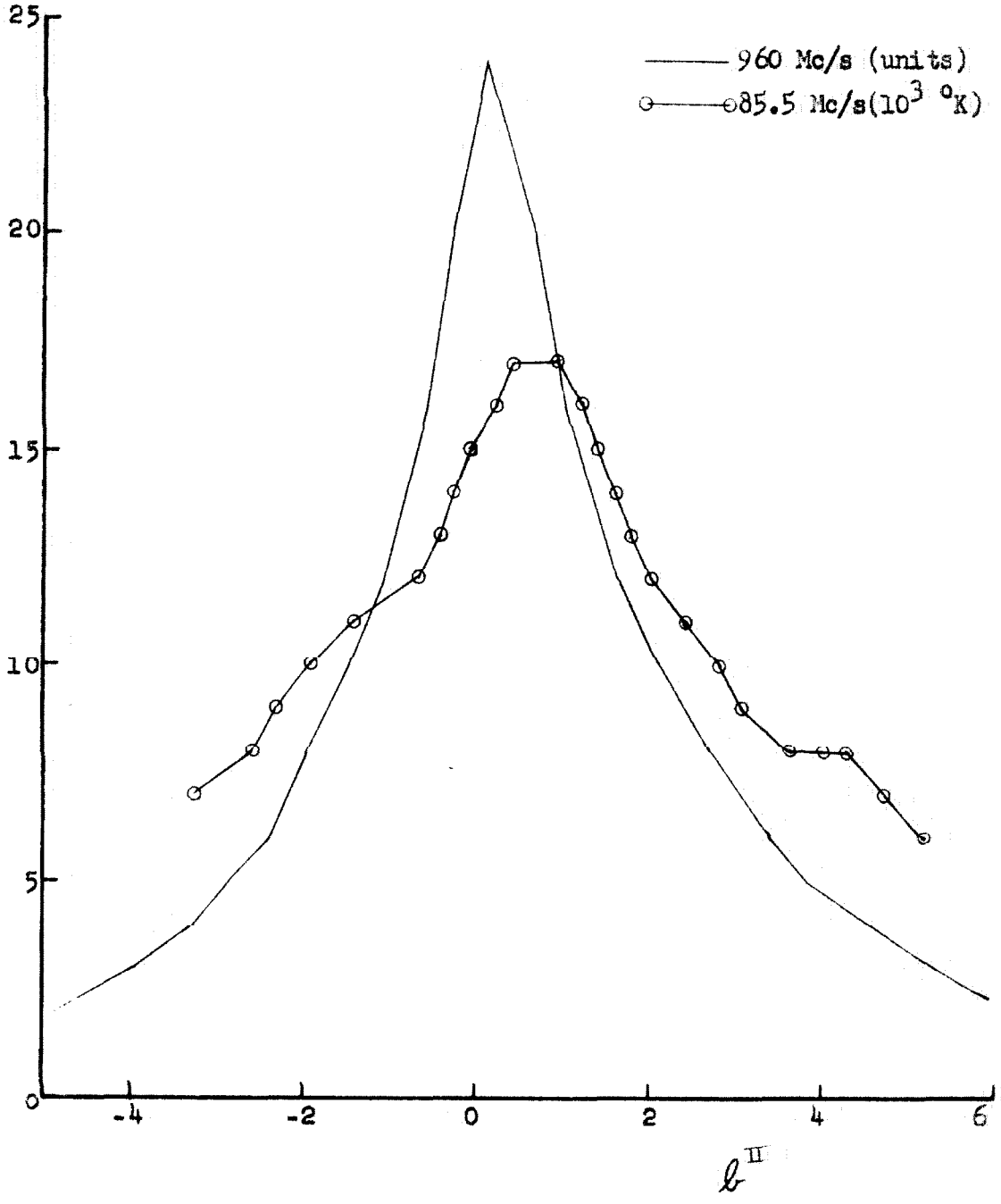

Figure 18. Cross sections of the 960 and 85.5 Mc/s surveys at $l^{II} = 355.3$.

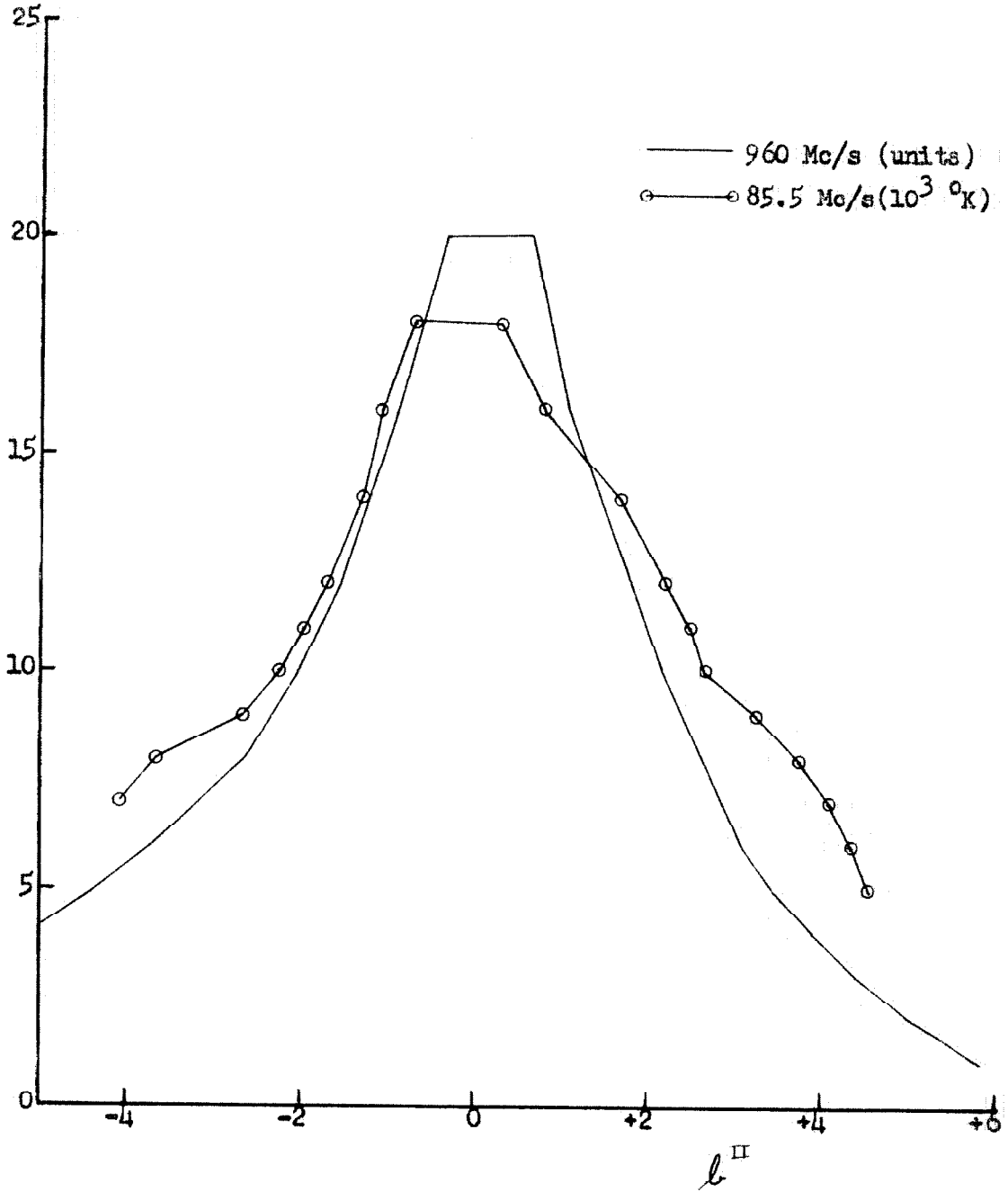

Figure 19. Cross sections of the 960 and 85.5 Mc/s surveys at $\ell^{II} = 4.^{\circ}3$.

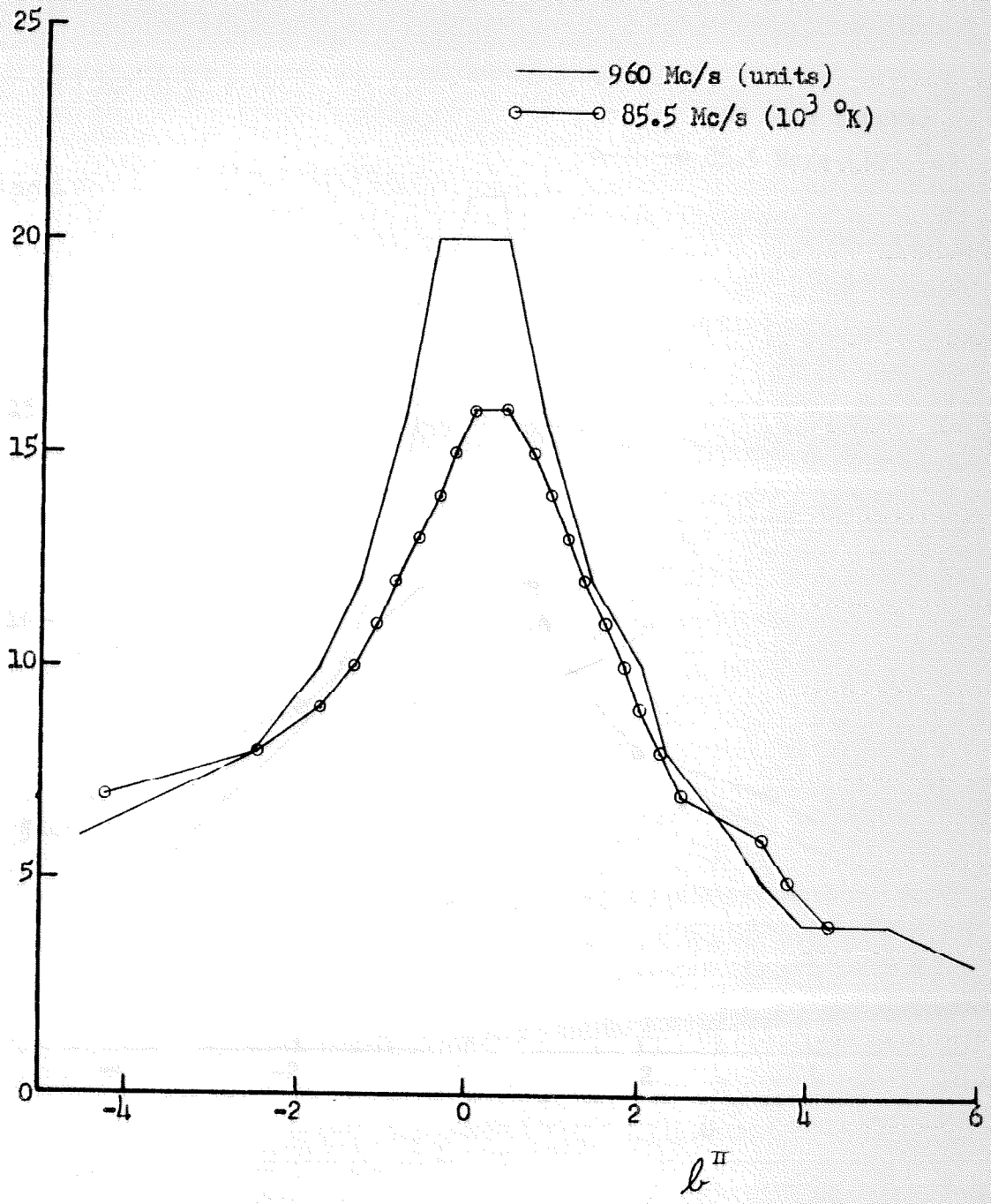

Figure 20. Cross sections of the 960 and 85.5 Mc/s surveys at $\ell^{II} = 11.^{\circ}3$.

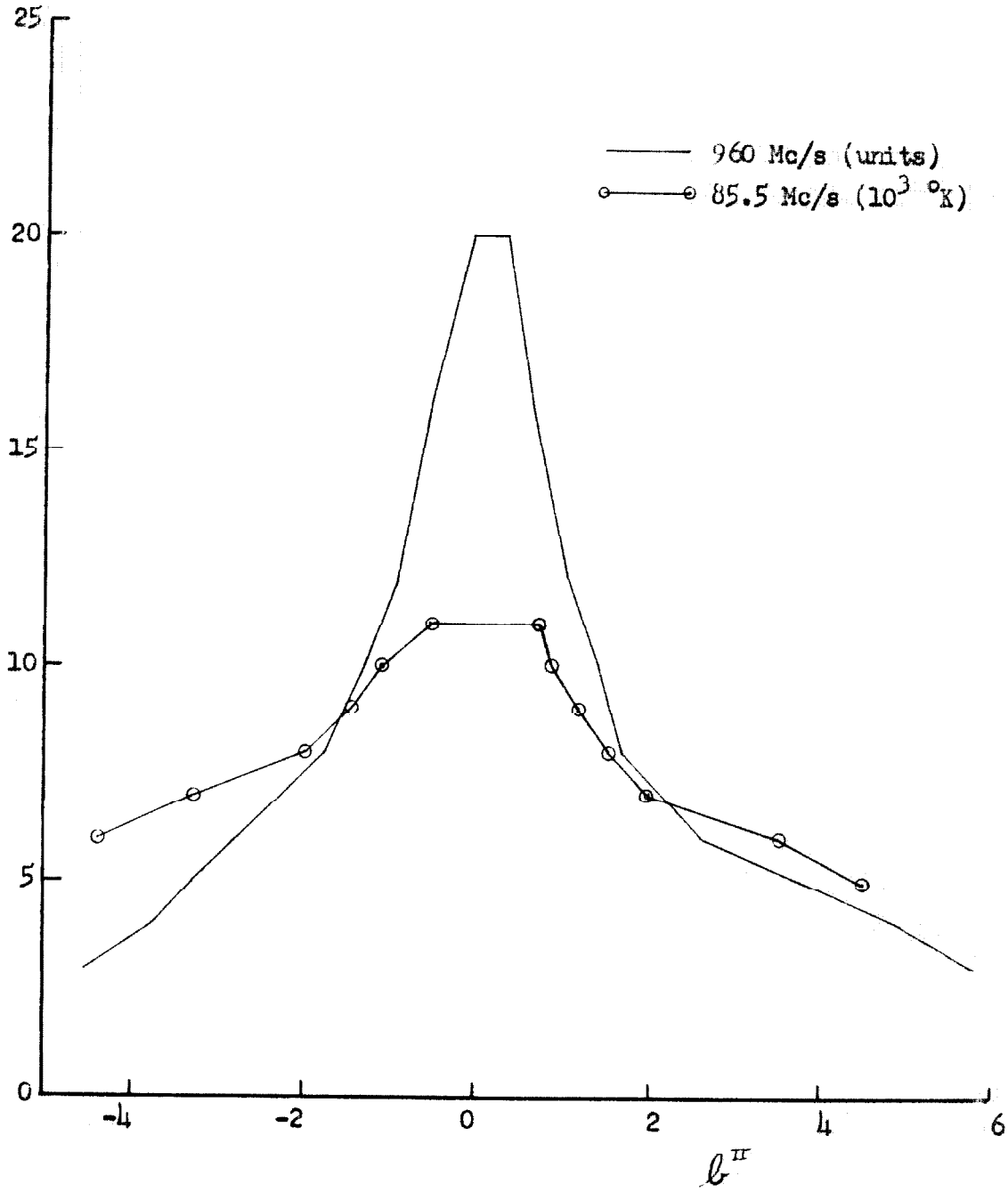

Figure 21. Cross sections of the 960 and 85.5 Mc/s surveys at $\ell^{II} = 26.^{o}3$.

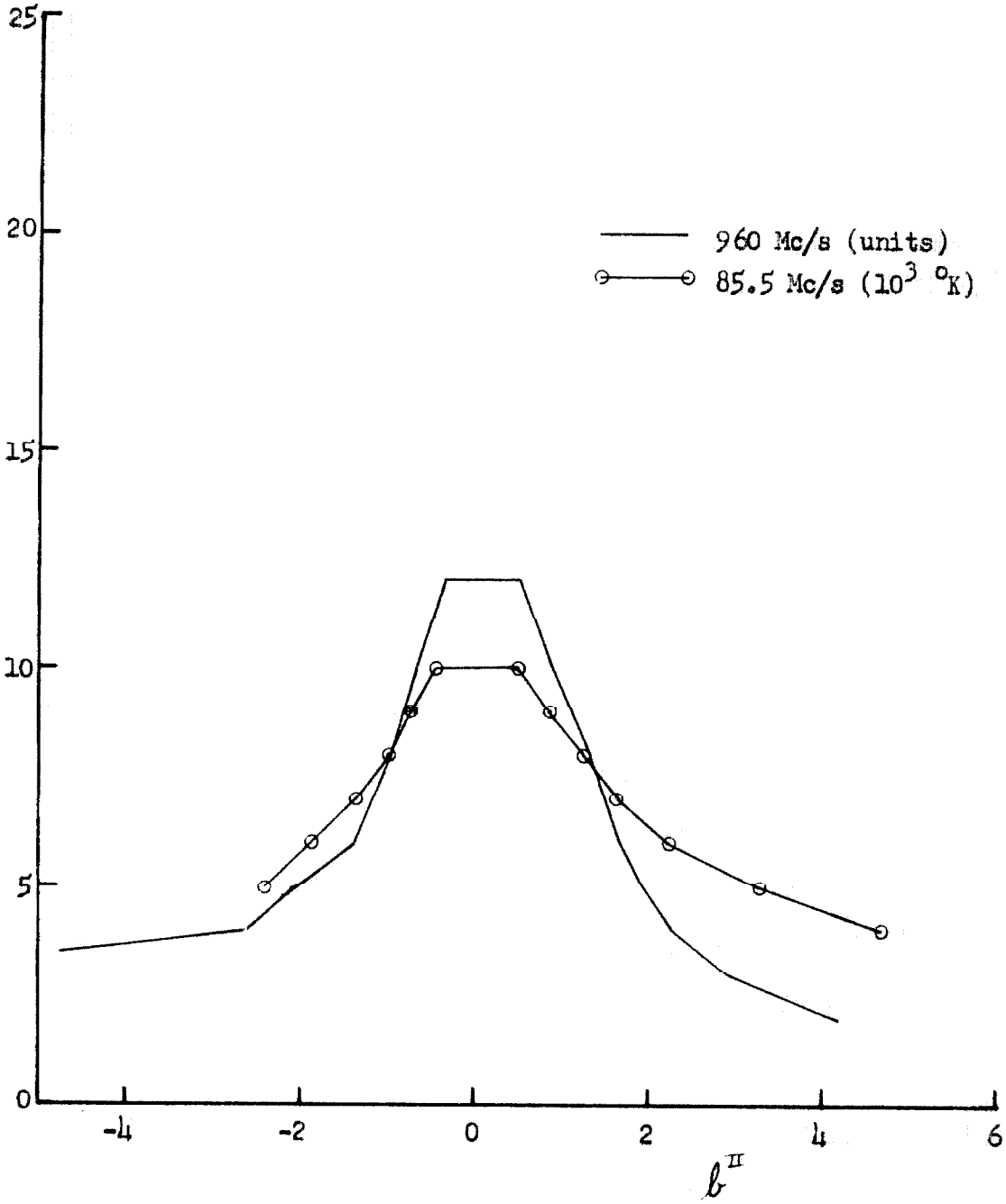

Figure 22. Cross sections of the 960 and 85.5 Mc/s surveys at $\ell^{II} = 36.^{\circ}3$.

these positions with the intensity scale modified as described in the section on the spectrum of discrete sources. Column 4 of this table gives the total temperature at 960 Mc/s for these positions, and column 5 the spectral index computed for these temperatures.

The usual interpretation of the radio radiation from the Galaxy is that it results from a mixture of two processes: free-free transitions in ionized hydrogen regions with a kinetic temperature of about $10,000^{\circ}K$, and synchrotron emission from high-energy electrons accelerated in the galactic magnetic field.

The spectrum of the free-free or thermal component is known. The optical depth is proportional to $\nu^{-2.1}$ in the radio frequency range under the usual physical conditions (50). The synchrotron process (non-thermal component) produces a power law spectrum also if the electron energy distribution is a power law (c. f. 51), but the power of the law (temperature spectral index) is not known.

At low frequencies the ionized hydrogen clouds are beginning to be optically thick. The resultant spectrum is therefore dependent on three things: the relative amount of thermal and non-thermal radiation, the spectral index of the non-thermal component, and the relative positions of the sources.

It is expected that the synchrotron electrons will be distributed fairly continuously throughout the plane of the Galaxy, but that the ionized hydrogen may be distributed in a somewhat clumpy fashion. Nevertheless, the assumption will be made in the following that the ratio of the two sources is constant along the line of sight, and that the

spectral index of the non-thermal radiation is constant throughout the plane. The equation of transfer may then be integrated to give the result (c. f. 22):

$$T = (T_e + \frac{T_n}{\tau})(1 - e^{-\tau}) \qquad (38)$$

where

τ is the total optical depth in ionized hydrogen along the line of sight

T_e is the electron temperature of the ionized hydrogen

T_n is the total temperature contributed along the line of sight by non-thermal radiation

T is the brightness temperature.

At frequencies above about 400 Mc/s the optical depth is sufficiently small that $1 - e^{-\tau} \approx \tau$. Therefore if ν_o is greater than 400 Mc/s, equation 38 can be approximated by:

$$T(\nu_o) = T_e \tau_o + T_{no} \qquad (39)$$

where τ_o is the optical depth at ν_o and T_{no} is the non-thermal component at ν_o. If the temperature spectral index of the non-thermal radiation is α, the brightness temperature at some other frequency ν_1 will be:

$$T(\nu_1) = [\, T_e \tau_o (\frac{\nu_o}{\nu_1})^{2.1} + T_{no} (\frac{\nu_o}{\nu_1})^{\alpha} \,] \, \frac{1 - e^{-\tau_o (\nu_o/\nu_1)^{2.1}}}{\tau_o (\nu_o/\nu_1)^{2.1}} \qquad (40)$$

The spectral index of the total radiation will be:

$$\alpha_o = \frac{\log \frac{T(\nu_1)}{T(\nu_o)}}{\log\left(\frac{\nu_o}{\nu_1}\right)} = \frac{\log\left[\frac{\left(\frac{\nu_o}{\nu_1}\right)^{2.1} + \beta\left(\frac{\nu_o}{\nu_1}\right)^{\alpha}}{1+\beta}\right] + \log f(\tau_o)}{\log\left(\frac{\nu_o}{\nu_1}\right)} \qquad (41)$$

where $\beta = T_{no}/10,000\tau_o$ is the ratio of thermal to non-thermal temperature at ν_o, and

$$f(\tau_o) = \frac{1 - e^{-\tau_o\left(\frac{\nu_o}{\nu_1}\right)^{2.1}}}{\tau_o\left(\frac{\nu_o}{\nu_1}\right)^{2.1}}$$

In terms of β the thermal components of the radiation are given by:

$$T_T(\nu_o) = \frac{T(\nu_o)}{1+\beta} = T_e\tau_o$$

$$T_T(\nu_1) = \frac{T(\nu_1)}{1 + \beta\left(\frac{\nu_o}{\nu_1}\right)^{\alpha-2.1}} = T_e\left(1 - e^{-\tau_o\left(\frac{\nu_o}{\nu_1}\right)^{2.1}}\right) \qquad (42)$$

Since $f(\tau_o)$ is about one, $\log f(\tau_o)$ is small, and equation 41 can be solved by an iterative procedure. First, $1/(1+\beta)$ and $1/[1+\beta(\nu_o/\nu_1)]^{\alpha-2.1}$ are plotted against the first term on the right side of equation 41. With this plot, an approximate value of $T_T(\nu_1)$ can be found from the observed spectral index and $T(\nu_1)$. The second term on the right side of equation 41 is found from a plot against $T_T(\nu_1)$ on another graph. This is entered as a change in the observed spectral index in the first plot, and the thermal component is recomputed, etc. After a little practice, the correct value of the correction can be guessed straight away, or with one iteration. The value of $1/(1+\beta)$ is then read off to give the 960 Mc/s thermal temperature.

The remaining variable in the separation into components is the spectral index of the non-thermal component. This has been found using the method suggested by Westerhout (22), who points out that if the ionized hydrogen is confined to the same thin disk as the neutral hydrogen, the thermal component will be small at $b^{I} = -6^{o}$ and $b^{I} = +4^{o}$ (the edges of Mill's map). The spectral index was therefore guessed to be about 2.4 from an examination of column 5 of table 6. The separation was then carried out with a special index of 2.40, and for comparison, 2.45. The thermal component at 960 Mc/s found in these two separations is shown in figures 23 and 24. The amount of negative thermal component seen in figure 23 indicates that 2.40 is probably too low. Columns 6 and 7 of table 6 give the thermal components at 85.5 and 960 Mc/s resulting from the separation using $\alpha = 2.45$.

The solid curve in figure 25 is a plot of the 960 Mc/s thermal component ($\alpha = 2.45$) versus longitude for $b^{II} = 0$. The value given for $l^{II} = 4^{o}.5$ is an average of the values at $l^{II} = 355^{o}.3$ and $4^{o}.3$. The extension of this curve beyond 45^{o} is a guess at the values in this region using the 400 Mc/s map. Figure 26 is a similar plot for the non-thermal component.

In order to convert these data into corresponding space distributions, a two-dimensional, circularly symmetrical model of the plane was constructed, having rings of constant emissivity 1/2 kpc wide in the inner regions and up to 2 kpc wide in the outer regions. The sun was taken to be 10 kpc from the center, and the emissivity was taken

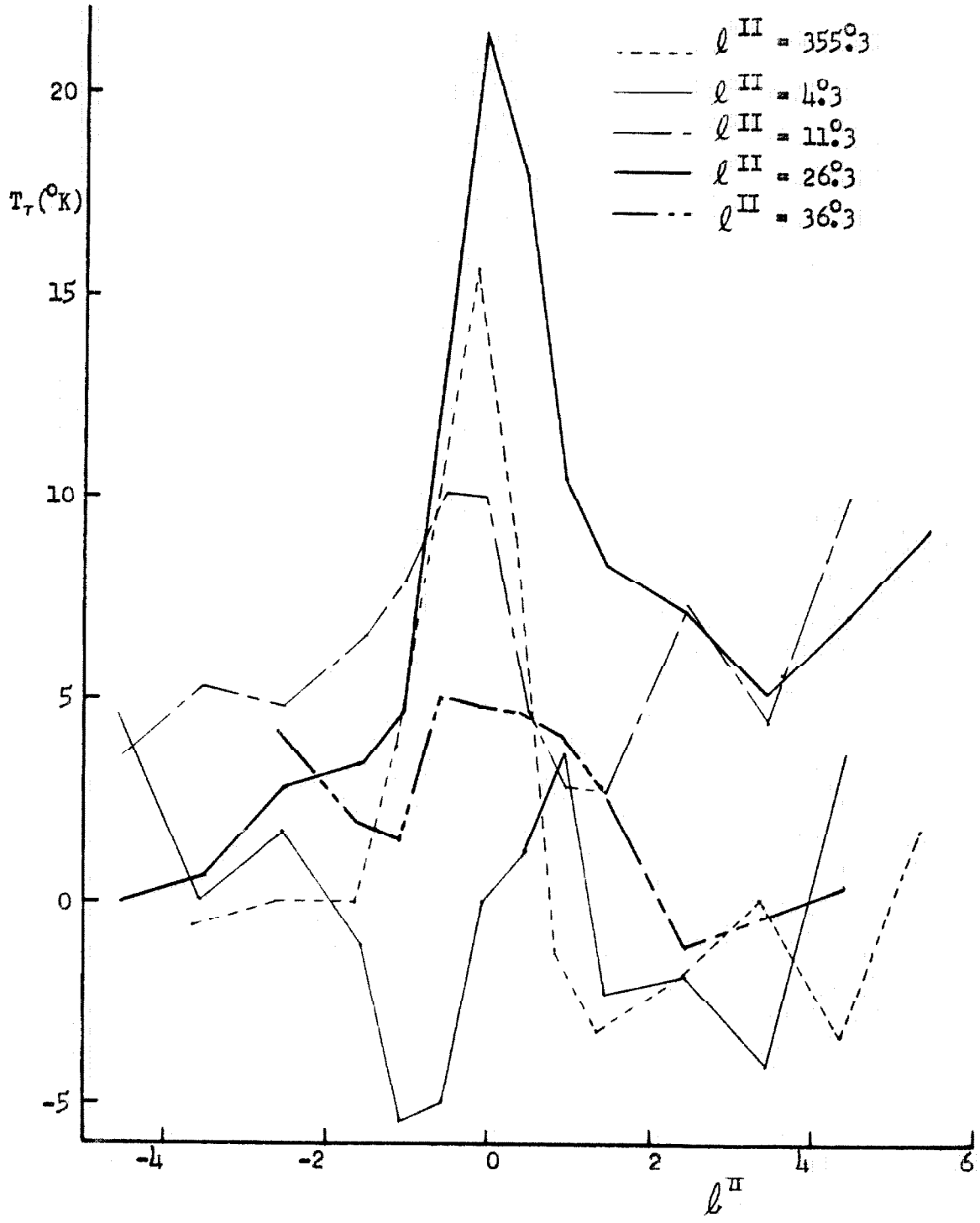

Figure 23. Thermal component at 960 Mc/s versus latitude for several longitudes assuming a non-thermal spectral index of 2.40.

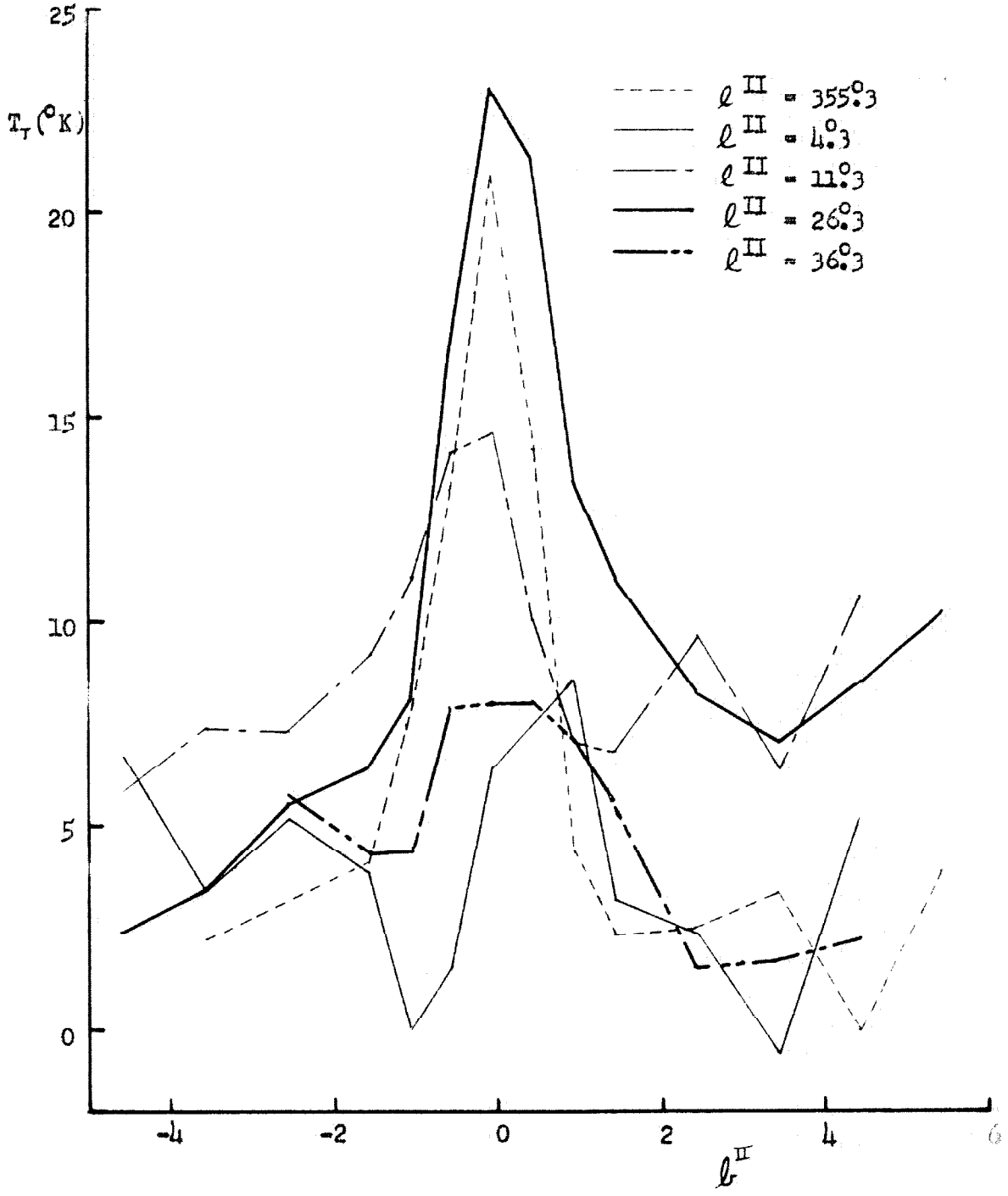

Figure 24. Thermal component at 960 Mc/s versus latitude for several longitudes assuming a non-thermal spectral index of 2.45.

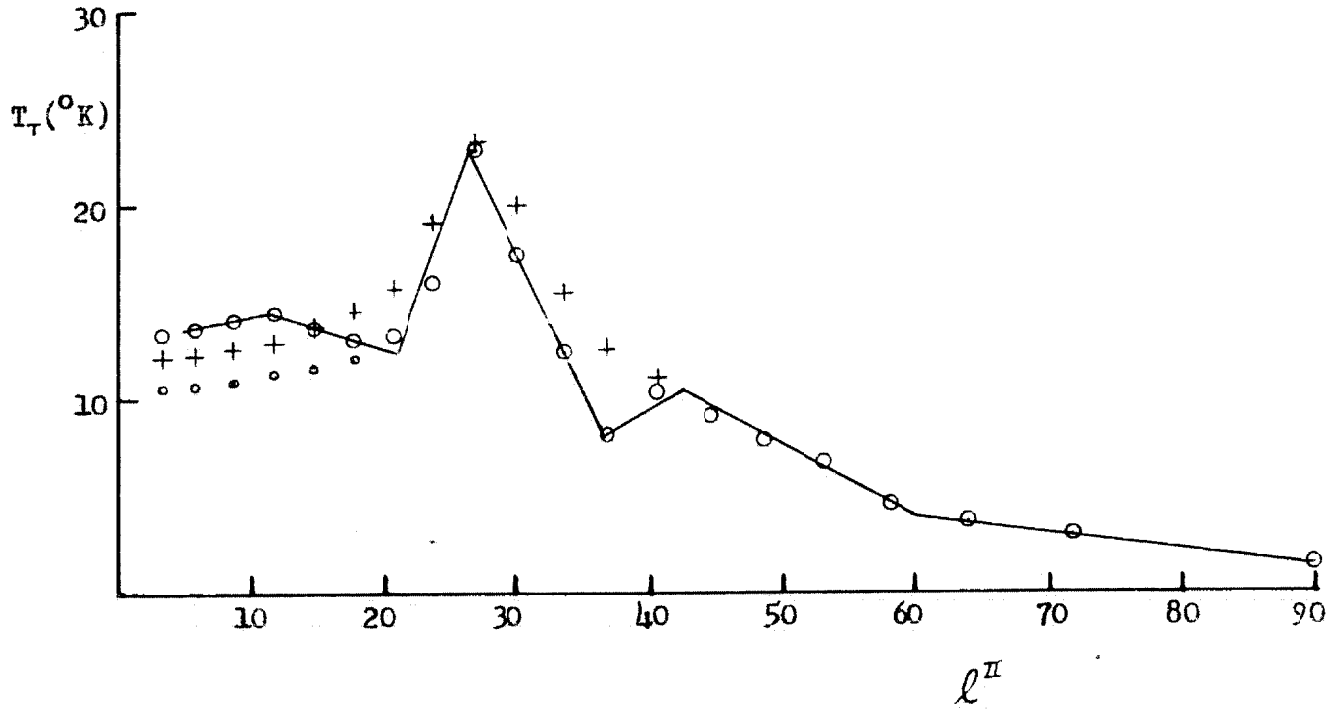

Figure 25. Intensity of thermal component at 960 Mc/s versus longitude for $b^{II} = 0$. The solid line represents the observed values. The large circles are computed from model A, the small circles from model B, and the crosses from model C.

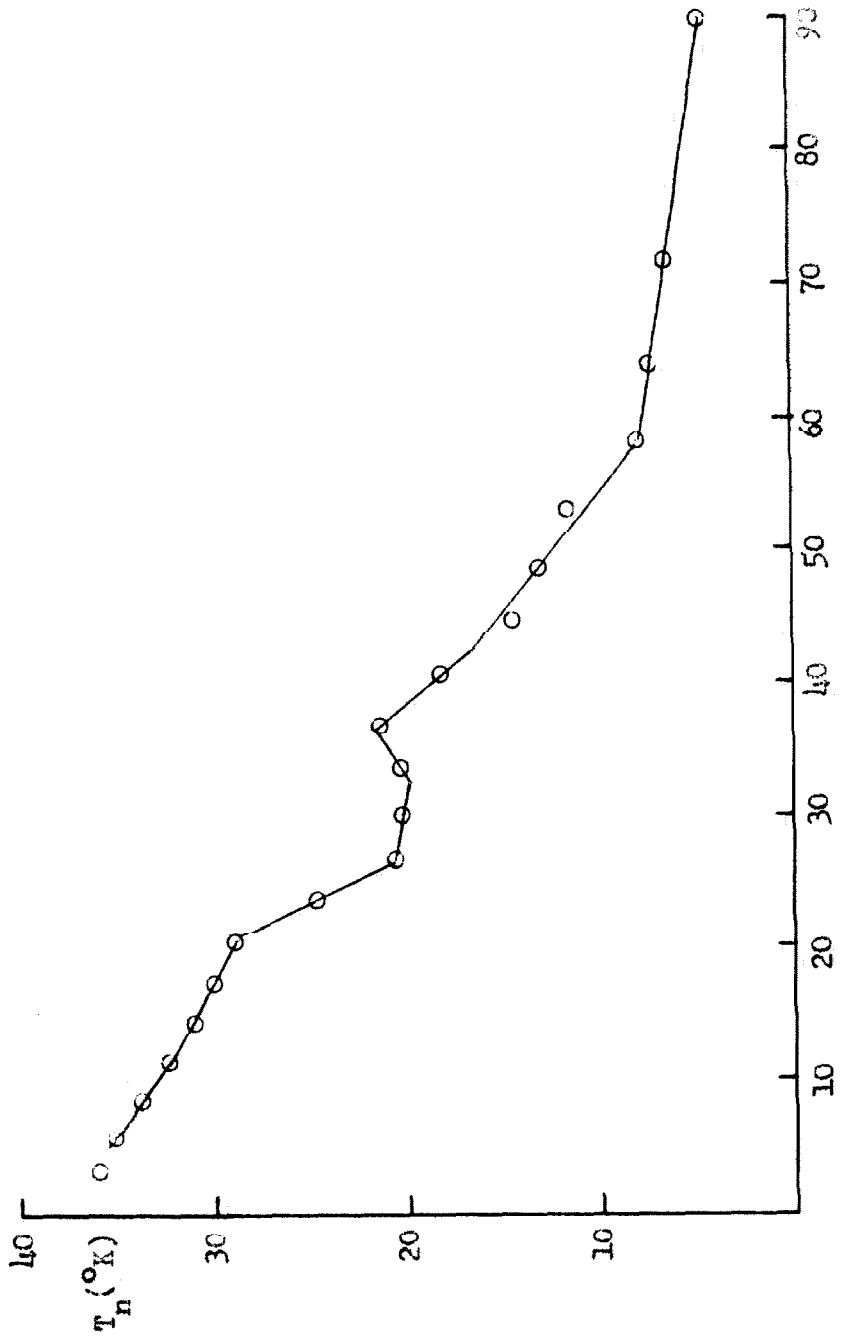

Figure 26. Intensity of non-thermal component at 960 Mc/s versus longitude for $b^{II} = 0$. The solid line represents the observed value and the circles are computed from a model.

to be zero outside 12 kpc. When this model was fitted to figures 25 and 26, the radial distributions shown in figure 27 (model A) and figure 28 resulted. The ordinate given on the left in both figures gives the emissivity in degrees Kelvin per kiloparsec. The circles in figures 25 and 26 are temperatures computed from the radial distribution model. These do not differ significantly from the observed data.

The thermal emissivity is seen to reach a definite peak at about 5 kpc. This maximum corresponds to the maximum found by Westerhout at 4 kpc. (He assumed the sun was 8 kpc from the center.) The other prominent feature of the distribution found by Westerhout--emissivity zero inside 2 kpc--is not found in the present data. To investigate the uncertainty in this result, two models were fitted with zero emissivity inside 3.5 kpc. The small circles and crosses in figure 25 show the fit to the data given by models B and C. In B, the emissivity outside 3.5 kpc has not been changed. In C, the peak at 5 kpc has been increased to partially compensate for the loss in the inner regions. The later model comes sufficiently close to the observed data that the possibility of zero emissivity inside 3.5 kpc cannot be excluded. The uncertainties in the inner regions of a model of this sort are always large, as only small deviations from circular symmetry in the outer regions of the Galaxy could completely change the conclusion to be drawn about the inner region.

In order to investigate the distribution of emissivity perpendicular to the galactic plane, average cross sections have been computed

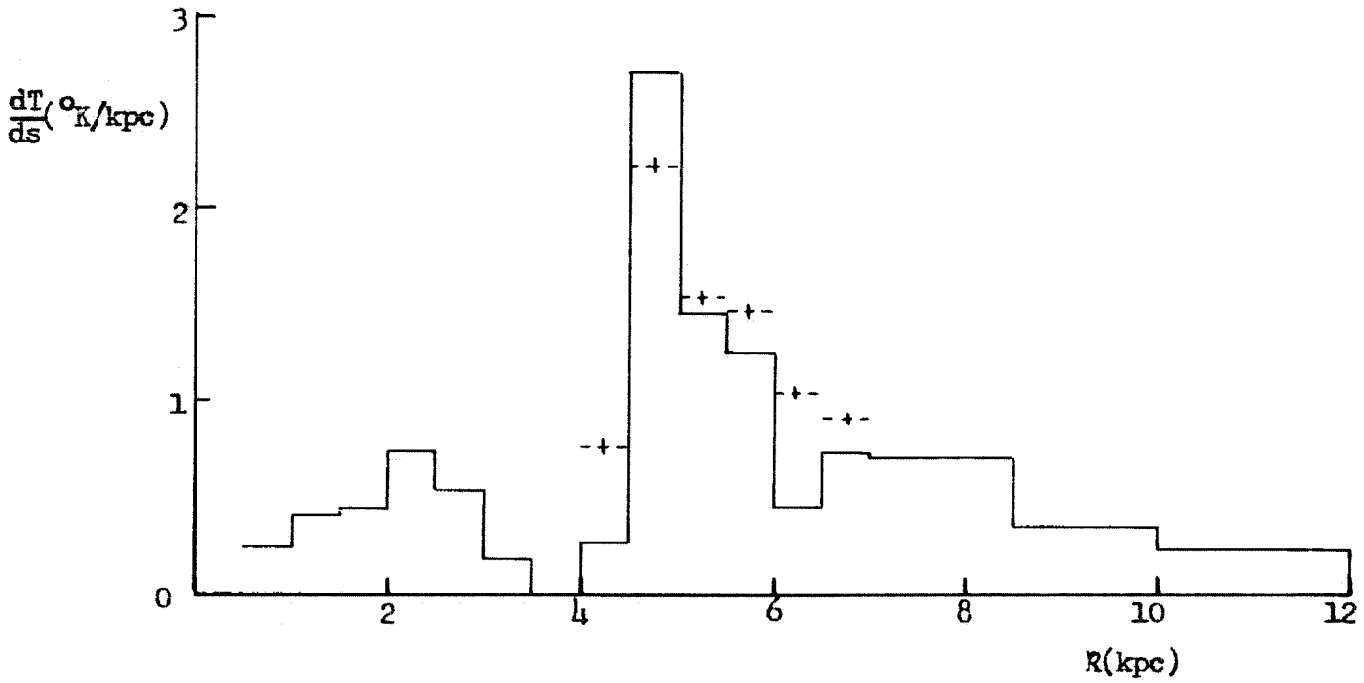

Figure 27. Radial distribution of thermal emissivity. The solid lines are model A. Models B and C are zero inside 4 kpc. Model B is otherwise the same as model A. Model C differs also as shown by the dotted lines with crosses.

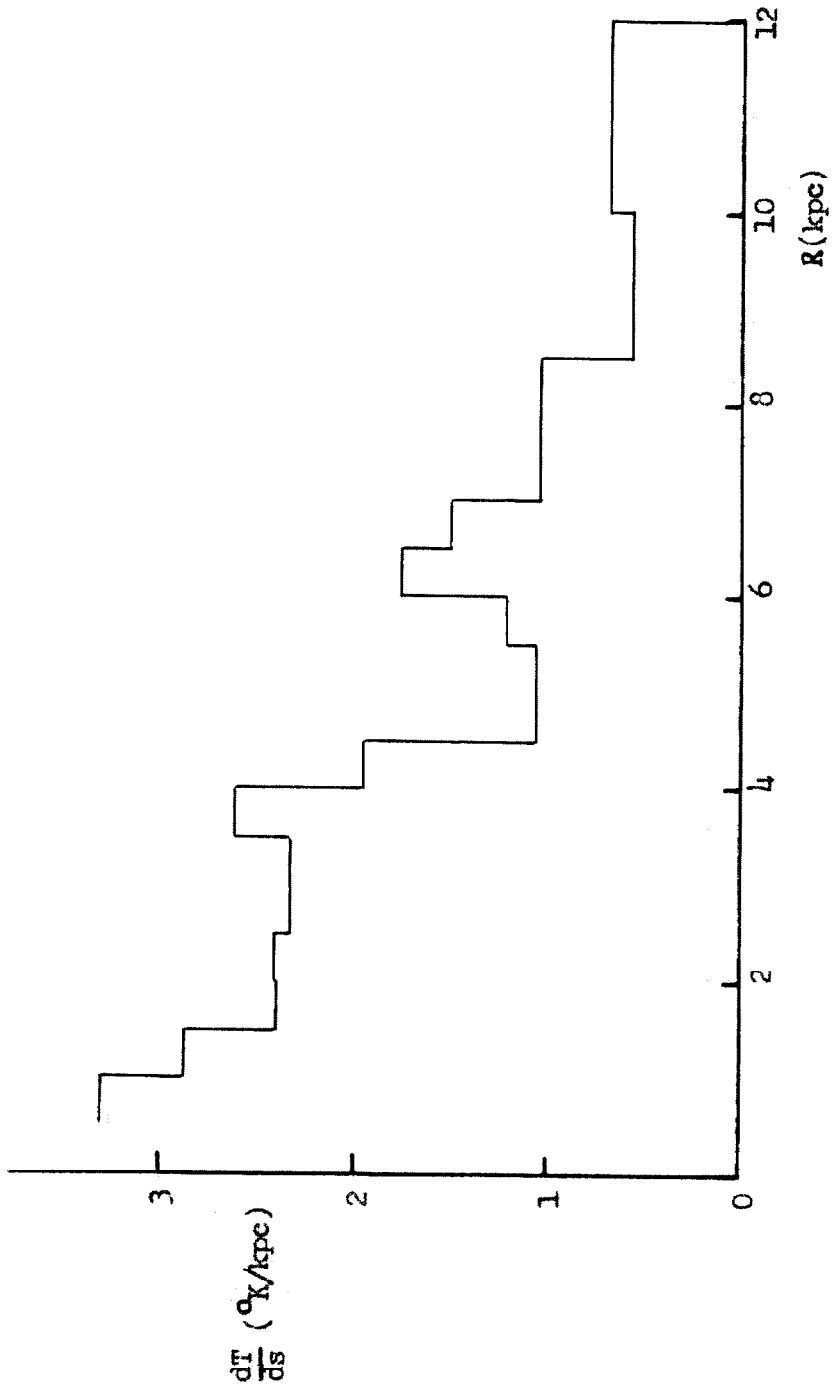

Figure 28. Radial distribution of non-thermal emissivity.

from the data in table 6 for both the thermal and non-thermal components. These are plotted in figures 29 and 30 as solid lines. The z-distribution of neutral hydrogen was found by Schmidt (54) to be approximately gaussian with full width at half maximum of 220 pc. (He used $R_\odot = 8$ kpc.) Since a similar sort of distribution might be expected to hold for ionized hydrogen, a model was computed using emissivity independent of R for $R < 12$ kpc (zero for $R > 12$ kpc) and a gaussian z-dependence with a width at half maximum of 275 pc. The circles in figure 29 are the best fit of this model to the data. A constant $2^\circ.8$ K has been added to the model to improve the fit. This change is approximately equivalent to changing the spectral index used for the non-thermal radiation by -0.05. A similar model fit to the non-thermal line is shown as circles in figure 30. The width at half maximum in this case is 840 pc.

Having found the distribution of emissivity due to ionized hydrogen, the distribution of the ionized hydrogen itself should follow. Scheuer (50) gives the absorption coefficient due to free-free transitions in ionized hydrogen as:

$$K = \frac{8\pi e^6 N_e N_i}{3c(2\pi mkT)^{3/2}\nu^2}\left(\ln \frac{8k^3T^3}{\pi^2 me^4\nu^2} - 5\gamma\right) \qquad (42)$$

where

N_e = number of electrons,

N_i = number of protons,

γ = 0.577... is Euler's number,

and the other symbols have their usual meaning.

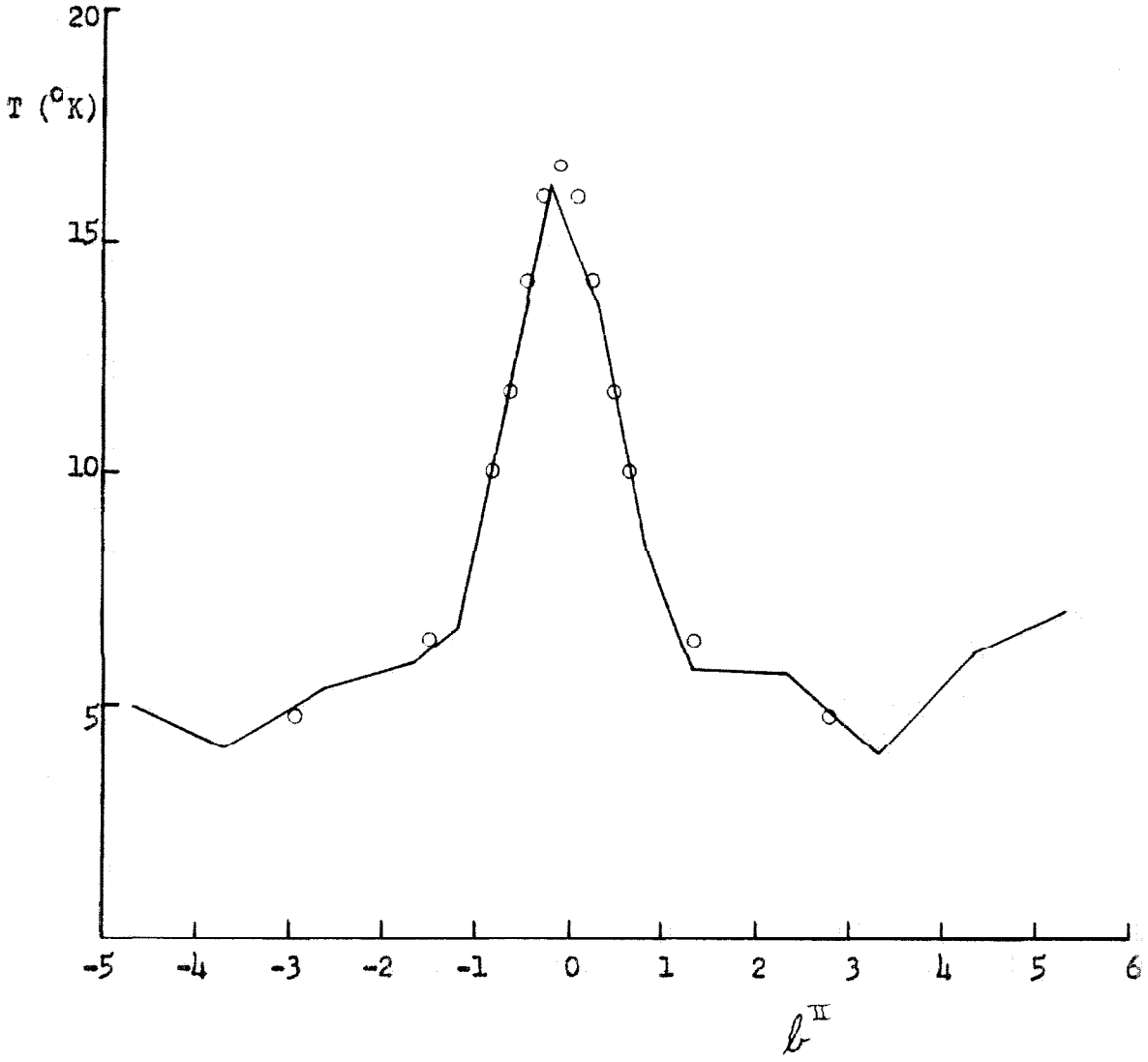

Figure 29. Average latitude distribution of thermal component at 960 Mc/s. The solid line is the observed value and the circles are from a model.

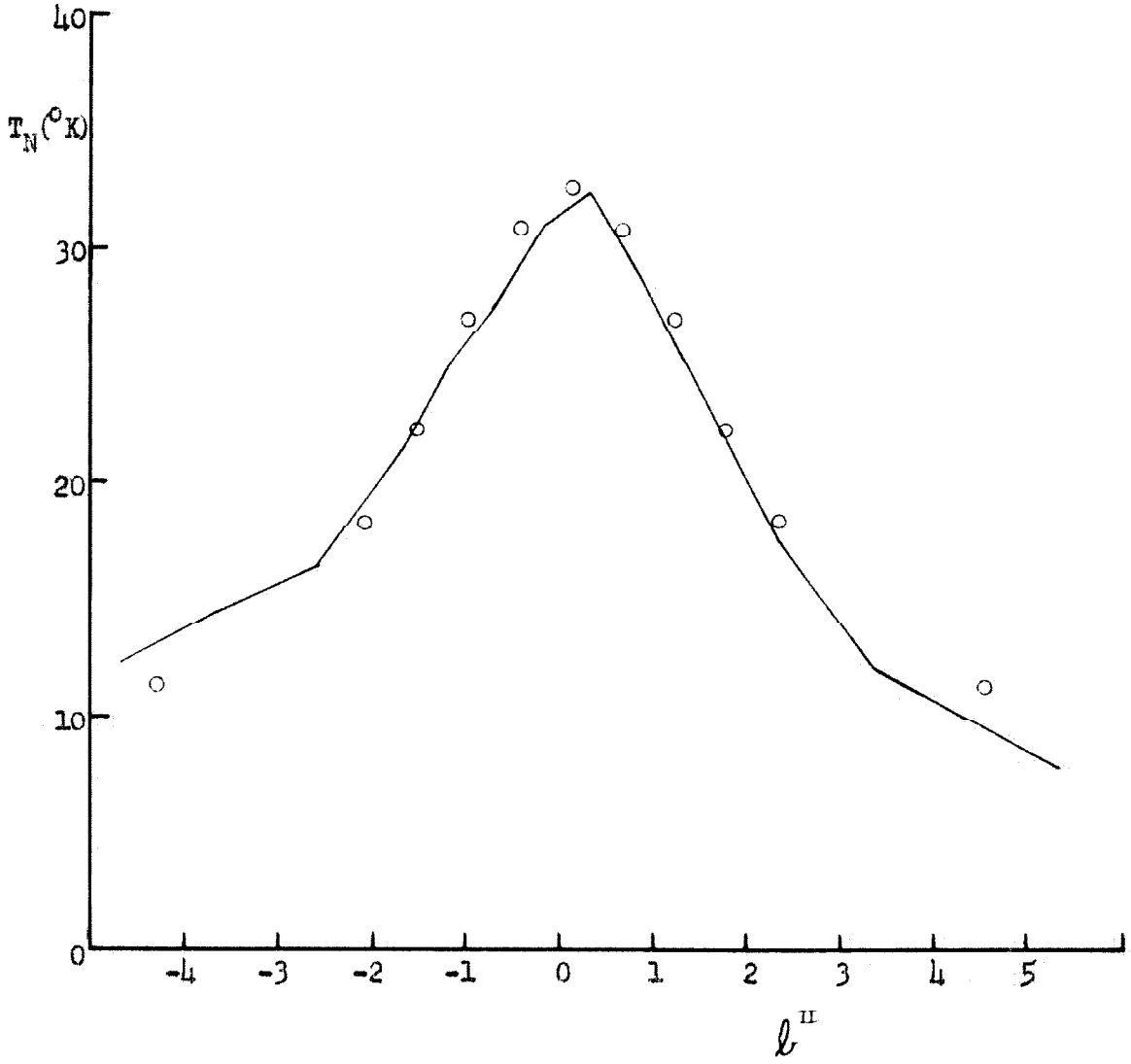

Figure 30. Average latitude distribution of non-thermal component at 960 Mc/s. The solid line is the observed value and the circles are from a model.

The kinetic temperature in ionized hydrogen regions is normally thought to be about 10,000°K, and the number of protons equal to the number of electrons (cf. 55). Using this figure, the absorption coefficient at 960 Mc/s becomes $K = 1.15 \times 10^{-25} N^2 \ (cm^{-1})$ where N is the number of electrons or protons. Since there are 3.085×10^{21} cm in a kpc,

$$\frac{dT}{ds} \left(\frac{^\circ K}{kpc}\right) = 3.55 \ N^2 \qquad (43)$$

and the emissivity in the solar neighborhood of about 0.3 °K/kpc found in the model corresponds to $N^2 = 0.08 \ cm^{-6}$. If this hydrogen is spread out evenly, the density of hydrogen is $N = 0.28 \ cm^{-3}$. It is much more likely, however, that the hydrogen is concentrated in clouds. Stromgren (55) suggests that such clouds may have an average density of 10 protons per cm^3, and the space between the clouds a density of several orders of magnitude smaller. If we consider a model in which clouds of density N_c occupy a portion a of the space, the average density of protons will be $n = aN_c$. In this model, a fraction a of the line of sight will be within a cloud where $N^2 = N_c^2$, and the rest of it will have $N^2 = 0$. The average emissivity will therefore be

$$\frac{dT}{ds} \left(\frac{^\circ K}{kpc}\right) = 3.55 \ aN_c^2 = 3.55 nN_c \qquad (44)$$

Using this model, the average density of protons in the solar neighborhood would be $0.08/N_c \ cm^{-3}$. We must, of course, require $N_c > 0.28 \ cm^{-3}$ in this region. Westerhout (56) finds that the density of neutral

hydrogen in the vicinity of the sun is about 0.5 cm^{-3}, so if we take Stromgren's figure of $N_c \geq 10$, the ratio of neutral hydrogen to ionized hydrogen in the solar region is about 60.

What has been done above for the solar neighborhood can, of course, be done in each of the rings. Furthermore, the model of the z-distribution gives an equivalent rectangular width of 294 pc for the rings, so the volume is known and the total mass of ionized hydrogen can be calculated. On the assumption that the hydrogen in each ring is spread uniformly, the mass is $6.93 \times 10^8 M_\odot$. Using the cloud model with N_c constant throughout the plane, the mass is $(3.85 \times 10^8 M_\odot)/N_c$ with the restriction that $N_c > 0.87$ cm^{-3}. Using Stromgren's value of $N_c = 10$ cm^{-3}, the mass is $3.58 \times 10^7 M_\odot$, or about 2.5% of the mass of neutral hydrogen found by Westerhout (56).

The emissivity produced by the synchrotron process is dependent on the electron flux and its variation with electron energy and the strength and orientation of the magnetic field. Biermann and Davis (52) have conveniently collected formulae for computing the radio emission by the synchrotron process. The assumption is made that the magnetic field is randomly oriented, and that the electron flux is proportional to some power of the electron energy. For 960 Mc/s radiation with a temperature spectral index of 2.45, the electron flux is related to the emissivity by:

$$N(>\tau) = 7.48(\overline{B}\gamma)^{-1.45}\tau^{0.9}\frac{dT}{ds} \qquad (43)$$

where:

$N(\tau)$ = electrons $cm^{-1}sec^{-1}sterrad^{-1}$ with energy greater than τ times the rest energy

$\tau = E/m_o c^2$ is the ratio of total energy to rest energy of the electrons

$\overline{B}\gamma$ = average magnetic field expressed in γ's (10^{-5} gauss)

$\frac{dT}{ds}$ = emissivity in ^{o}K/kpc.

The observed emissivity of 0.57^{o}K/kpc in the solar neighborhood requires a magnetic field of about 1γ to keep the electron flux within the limit suggested by Biermann and Davis. If we assume that the value of the electron flux taken for the solar neighborhood applies throughout the plane, the magnetic field must increase with decreasing R. The value reached in the inner regions would be around 3γ if the value near the sun is 1γ.

REFERENCES

1. Jansky, K. G. 1932, Proc. IRE, 20, 1920.

2. Hey, J. S., Parsons, S. J., and Phillips, J. W. 1946, Nature, 158, 234.

3. Bracewell, R. N. and Roberts, J. A. 1954, Aust. J. Phys., 7, 615.

4. Seeger, C. L., Westerhout, G., and van de Hulst, H. C. 195 B.A.N., 8, 89 (No. 472).

5. Dicke, R. H. 1956, Rev. Sci. Instr., 17, 268.

6. Westerhout, G. 1956, B.A.N., 13, 105 (No. 472).

7. Mezger, P. G. 1958, Zs. fur Ap., 46, 234.

8. Adgie, R. and Smith, F. G. 1956, Obs., 76, 181.

9. Seeger, C. L. 1956, B.A.N., 13, 100 (No. 472).

10. Bolton, J. G., Stanley, G. J., and Slee, O. B. 1954, Aust. J. Phys., 7, 110.

11. Denisse, J. F., Lequeux, J. and LeRoux, E. 1957, Compt. Rend., 244, 3030.

12. Grebenkemper, R., McClain, E. F., and Hagen, J. P. 1957, I.A.U. Symposium no. 4 (Cambridge at the University Press), 142.

13. Brown, R. H. and Hazzard, C. 1953, M.N., 113, 123.

14. Hagen, J. P., McClain, E. F., and Hepburn, N. 1954, Proc. IRE, 42, 1811.

15. Haddock, F. T., Mayer, C. M. and Sloanaker, R. M. 1954, Ap. J., 119, 456.

16. Haddock, F. T. and McCullough, T. P. 1955, A.J., 60, 161.

17. Jennison, R. C. and Lovell, A. C. B. 1956, Phil. Mag. Ser. 8, 1, 725.

18. Krauss, J. D., Ko, H. C. and Matt, S. 1954, A.J., 59, 439.

19. Little, A. G. 1958, Aust. J. Phys., 11, 1958.

20. Piddington, J. H. and Trent, G. H. 1956, Aust. J. Phys., 9, 74.

21. Razin, V. A. and Pletchkov, V. M. 1957, I.A.U. Symposium No. 4 (Cambridge at the University Press) 155.

22. Westerhout, G. 1958, B.A.N., 9, 215 (No. 488).

23. Broten, N. W. and Medd, W. J. 1960, Ap. J., 132, 279.

24. Alsop, L. E. et al. 1958, Paris Symposium on Radio Astronomy (Stanford University Press) 69.

25. Sloanaker, R. M. and Nichols, J. H. 1960, NRL Report 5485 (U.S. Naval Research Laboratory, Washington, D.C.).

26. Muller, H. G. 1959, Publications of the University Observatory at Bonn No. 52.

27. Private communitation from K. W. Linnes.

28. Davies, R. D. and Jennison, R. C. 1960, The Observatory, 80, 74.

29. Kajdanouski, N. L., Kardosev, N. S., and Sklovski, I. S., 1955, Kokl. Akad. Nauk., 104, 517.

30. Struve, O. 1960, A.J., 65, 546.

31. Harris, D. E. and Roberts, J. A. 1960, Pub. A.S.P., 72, 237.

32. Annals of the Obs. of Lund No. 16, 1951.

33. Wilson, R. W., and Bolton, J. G. 1960, Pub. A.S.P., 72, 331.

34. Kuzmin, A.D. Levchenko, M. T., Noskova, R.I., and Salomonovich 1960, Astronomicheskii Zhurnal, 37, 975.

35. Edge, D. O. et al. 1959, Mem. R.A.S., 68, 37.

36. Mills, B.Y., Slee, O.B., Hill, E.R. 1960, Aust. J. Phys., 13, 676.

37. Rishbeth, H. 1956, Aust. J. Phys., 9, 494.

38. Prazessions-Tatelen 1927 (The Hamberg Observatory in Bergdorf: The Observatory Press.

39. Zweiter Katalog der Astronomischen Gesellshaft 1951 (The Hamburg Observatory in Bergdorf: The Observatory Press).

40. Boss, B. General Catalogue of 33342 Stars For the Epoch 1950 (Published by the Carnegie Institution of Washington).

41. Sharpless, S. 1960, Ap. J. Supp. Ser., 4, 257.

42. Gum, C. S. 1955, Mem. R.A.S., 67, 155.

43. Lynds, C. R. 1961, Pub. of N.R.A.O., 1, 43.

44. Read, R. B. 1961, Trans. I.R.E., AP-9, 31.

45. Moffet, A. T. 1962, Submitted to Ap. J. (In Press).

46. Maltby, P. 1962, Submitted to Ap. J. (In Press).

47. Mills, B. Y. 1958, Paris Symposium on Radio Astronomy (Stanford University Press) 431.

48. Harris, D. E. 1961, Thesis (California Institute of Technology).

49. Hill, E. R., Slee, O.B., and Mills, B.Y. 1958, Aust. J. Phys., 11, 530.

50. Seeger, C.L., Stumpers, F.L.H.M., and van Hurch, N. 1960, Philips Tech. Rev., 21, 317.

51. Schever, P.A.G. 1960, M.N.R.A.S., 120, 231.

52. Biermann, L., and Davis Jr., L. 1960, Zs. fur Ap., 51, 19.

53. Henize, K.G. 1959, A.J., 64, 51.

54. Westerlund, B., private communication.

55. Schmidt, M. 1957, B.A.N., 13, 247 (No. 475).

56. Stromgren, B. 1949, Problems of Cosmical Aerodynamics, (C.A.D.O., Dayton, Ohio) 7.

57. Westerhout, G. 1957, B.A.N., 13, 201 (No. 475).

APPENDIX I

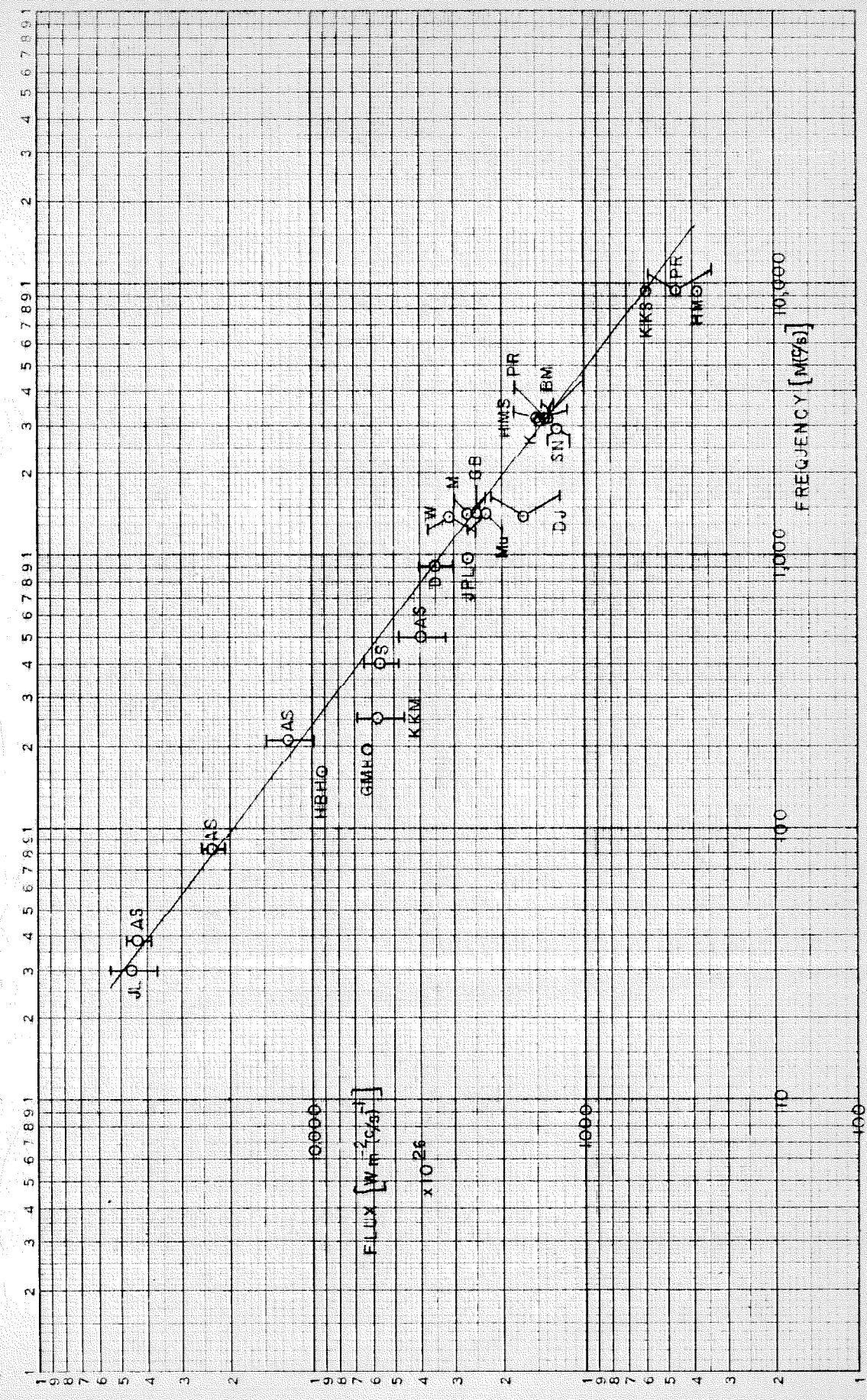

Figure 5. Absolute flux measurements of Cas A. The abbreviations are explained in Table I.

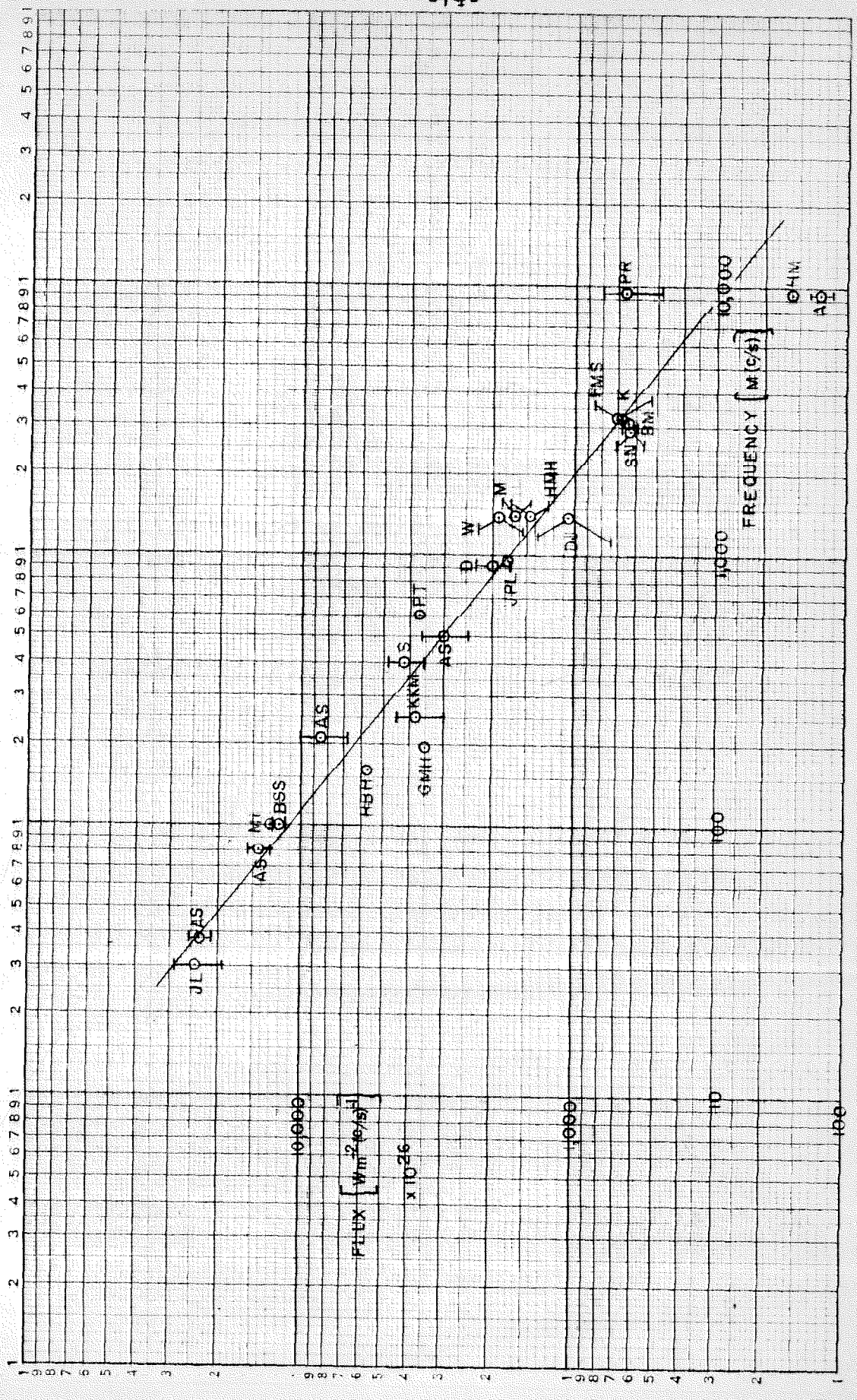

Figure 6. Absolute flux measurements of Cyg A. The abbreviations are explained in Table I.

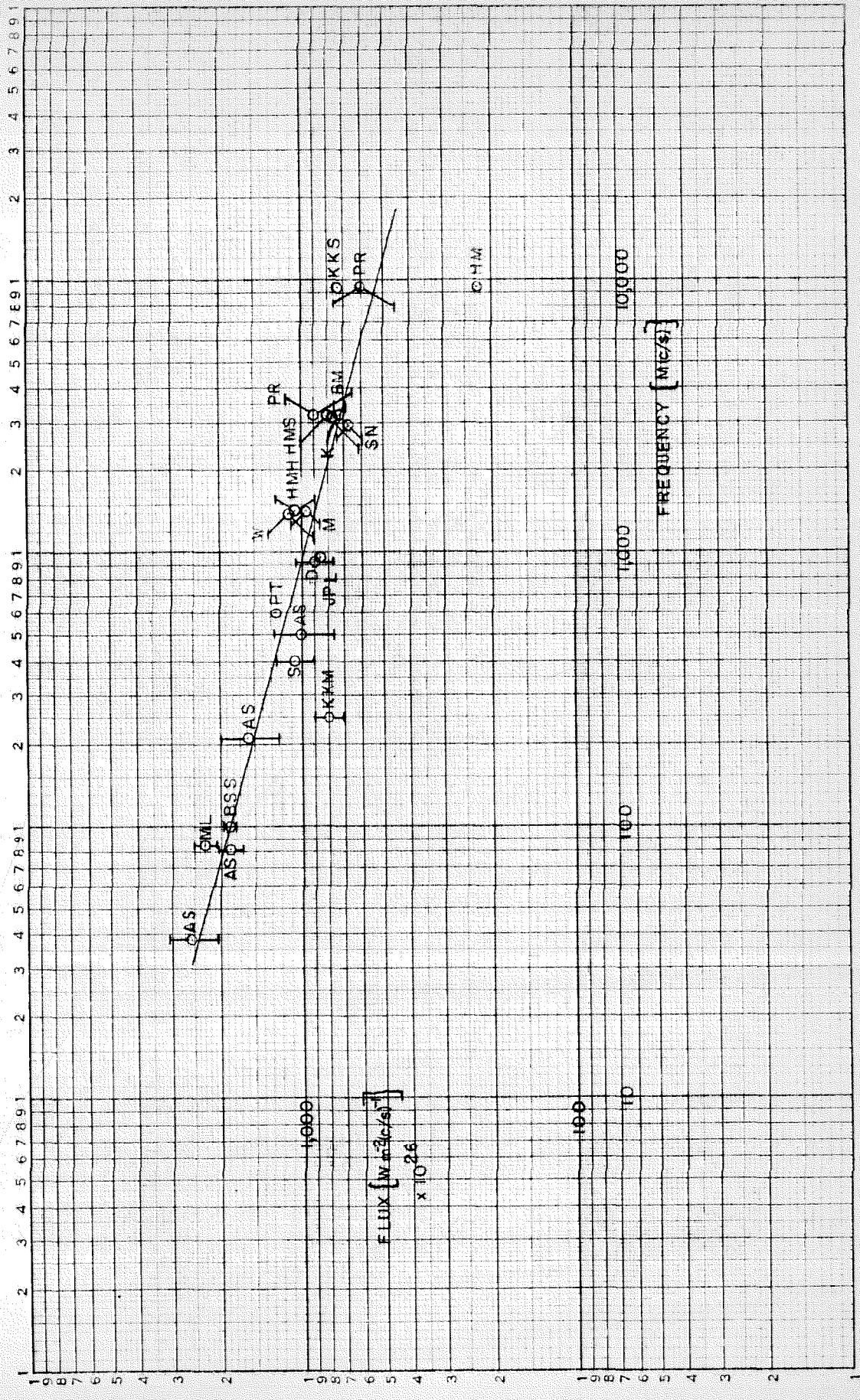

Figure 7. Absolute flux measurements of Tau A. The abbreviations are explained in Table I.

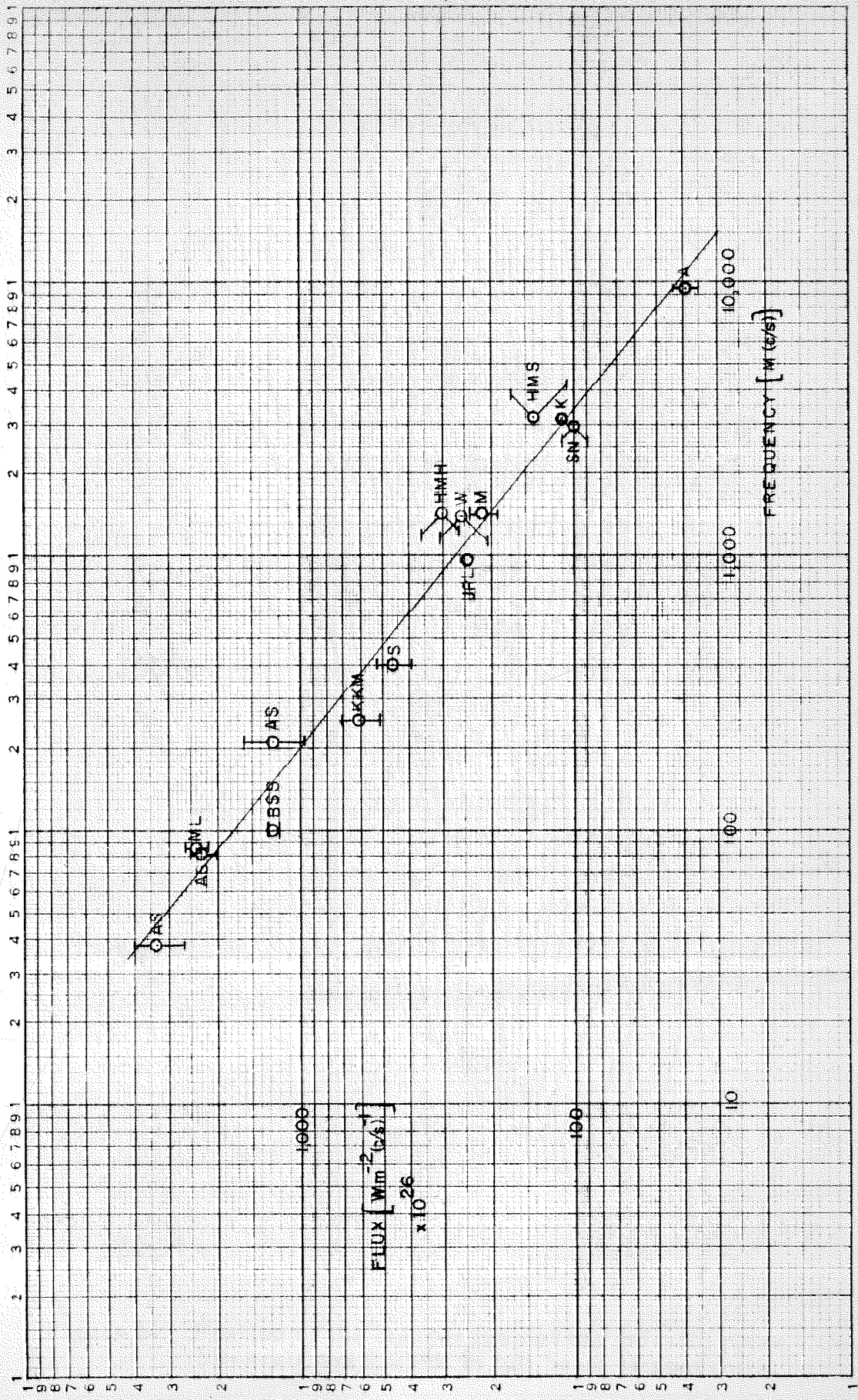

Figure 8. Absolute flux measurements of Vir A. The abbreviations are explained in Table I.

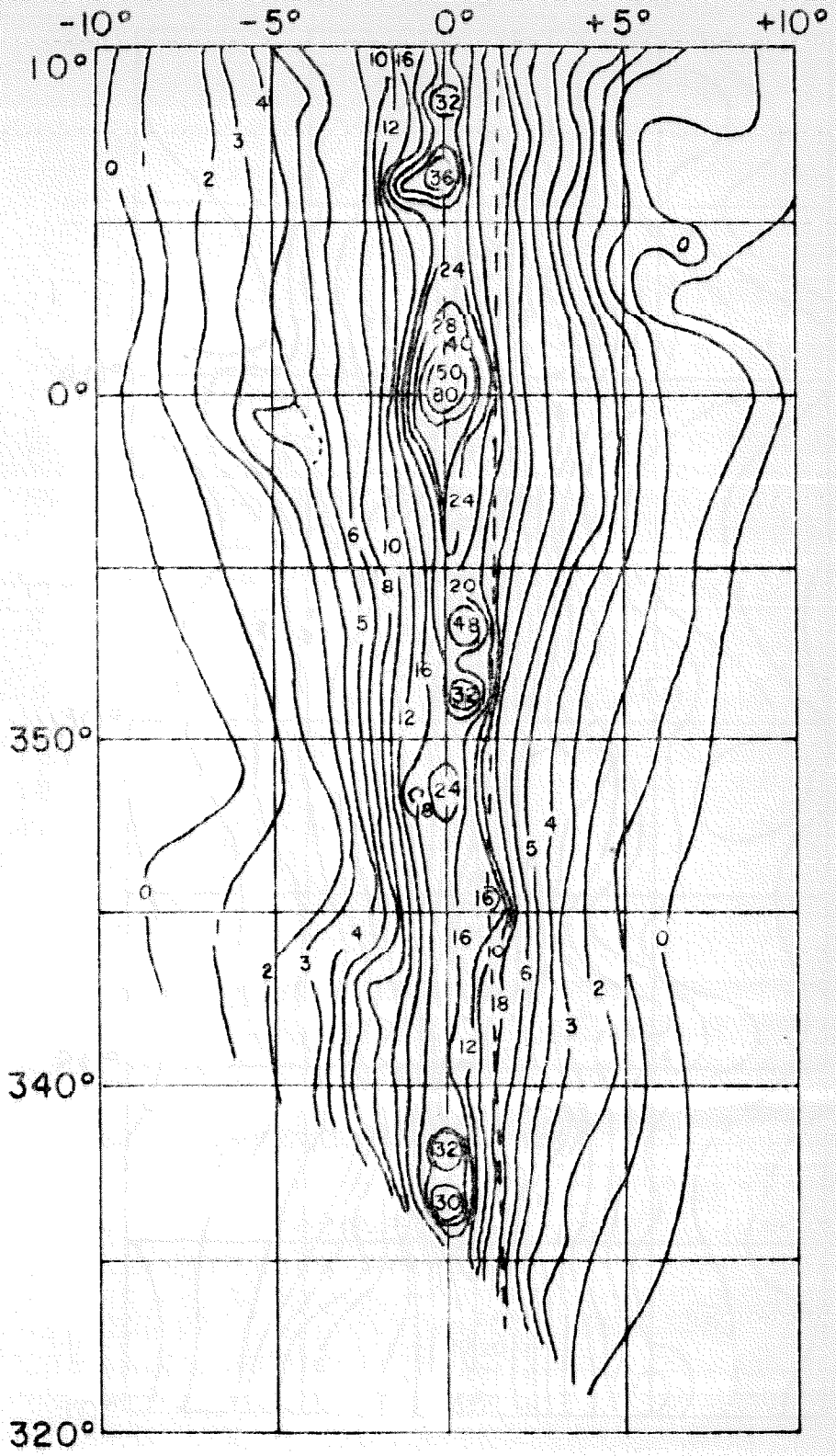

Figure 10. Portion of the contour map of the galactic plane. Contour intervals are 1.85°K in full beam temperature.

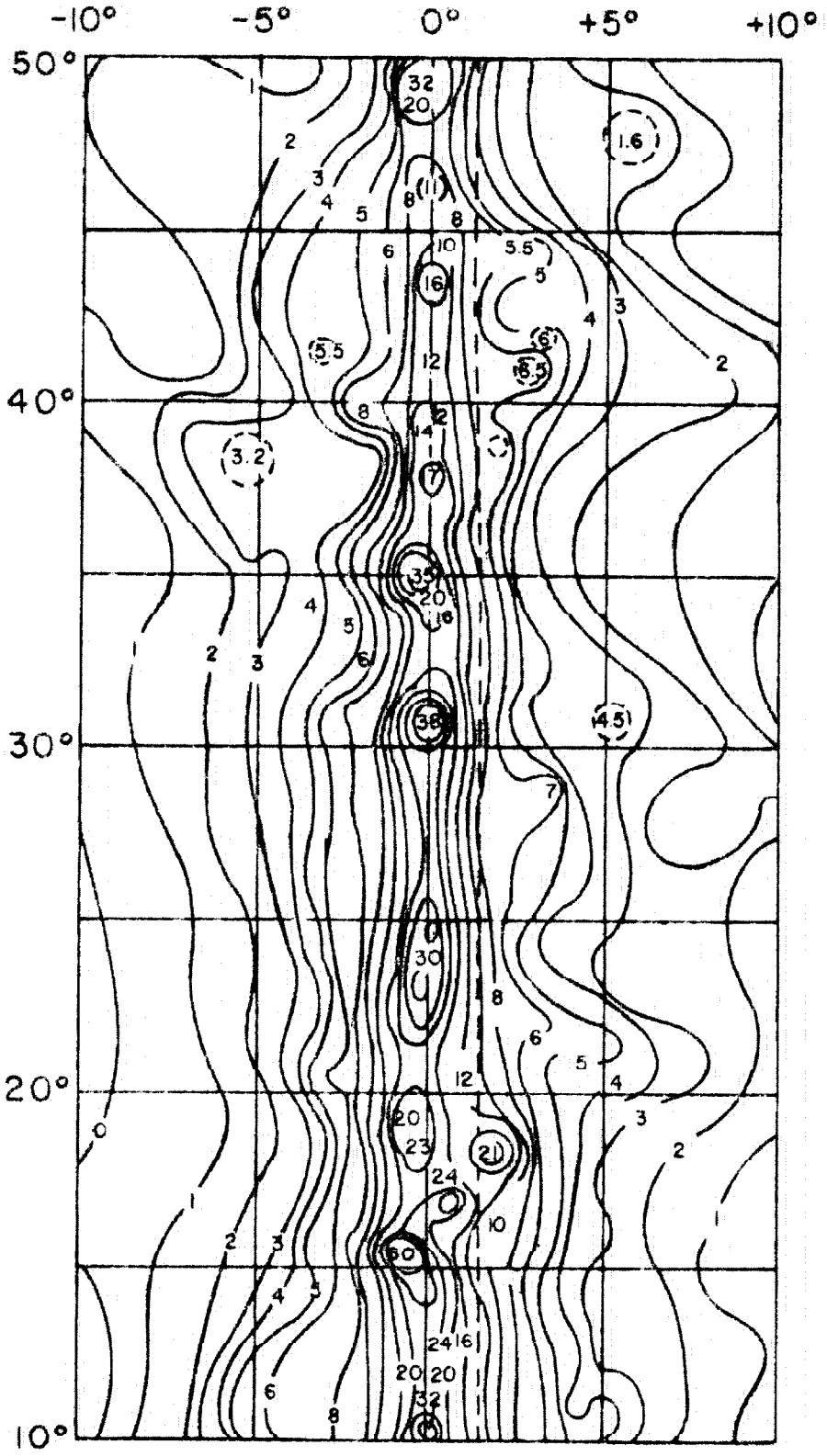

Figure 11. Portion of the contour map of the galactic plane. Contour intervals are 1.85°K in full beam temperature.

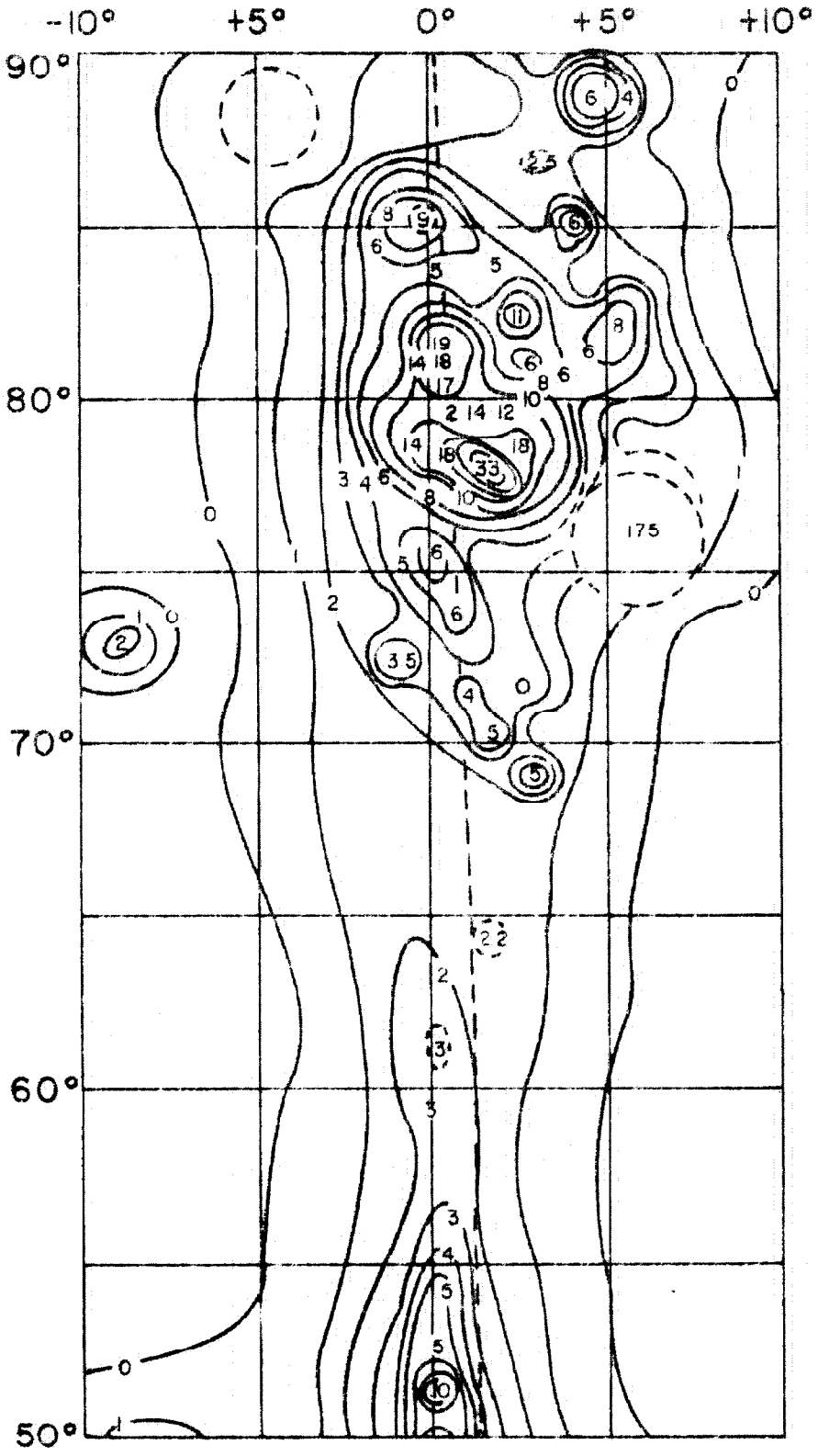

Figure 12. Portion of the contour map of the galactic plane. Contour intervals are 1.85°K in full beam temperature.

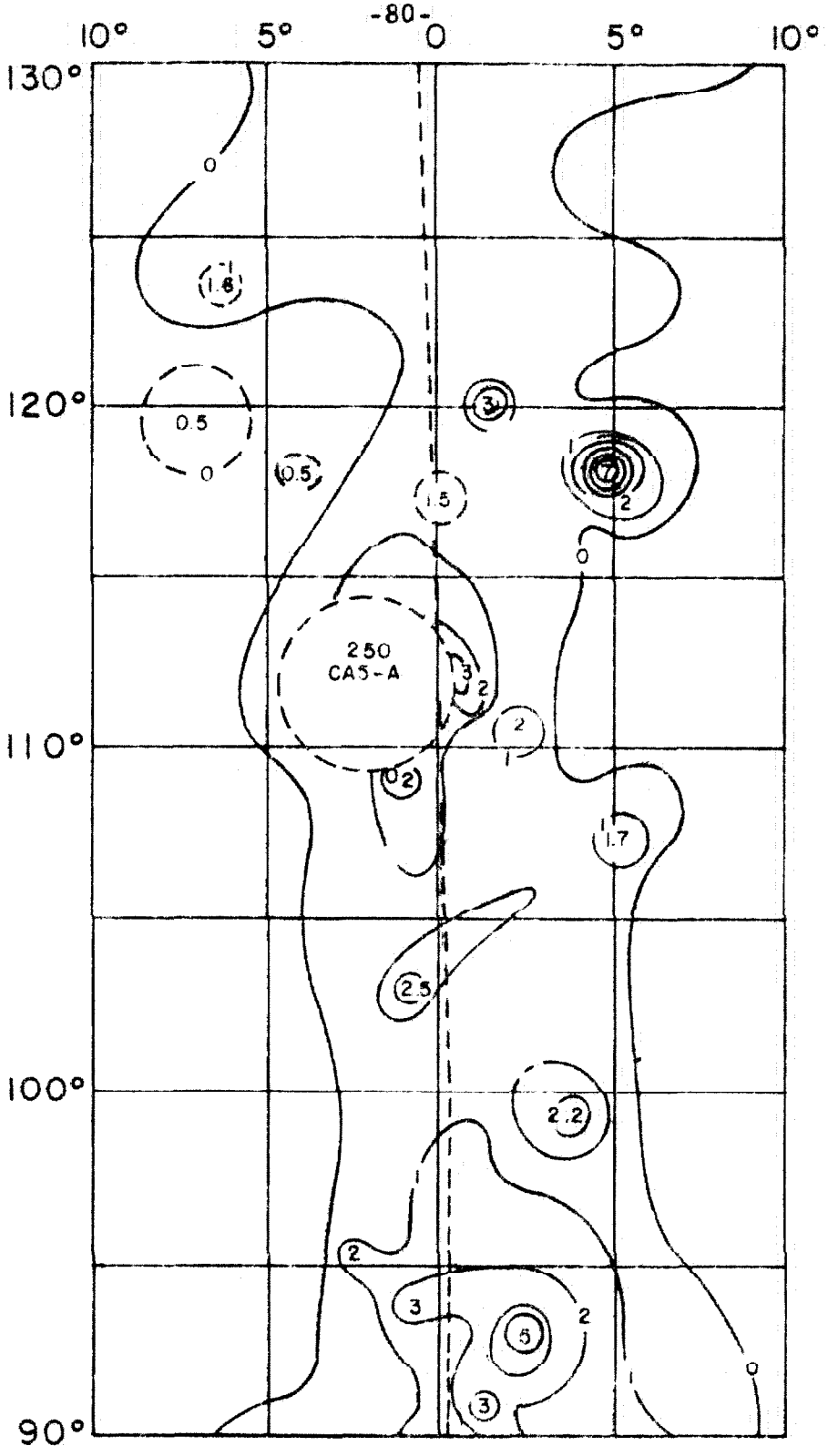

Figure 13. Portion of the contour map of the galactic plane. Contour intervals are 1.85°K in full beam temperature.

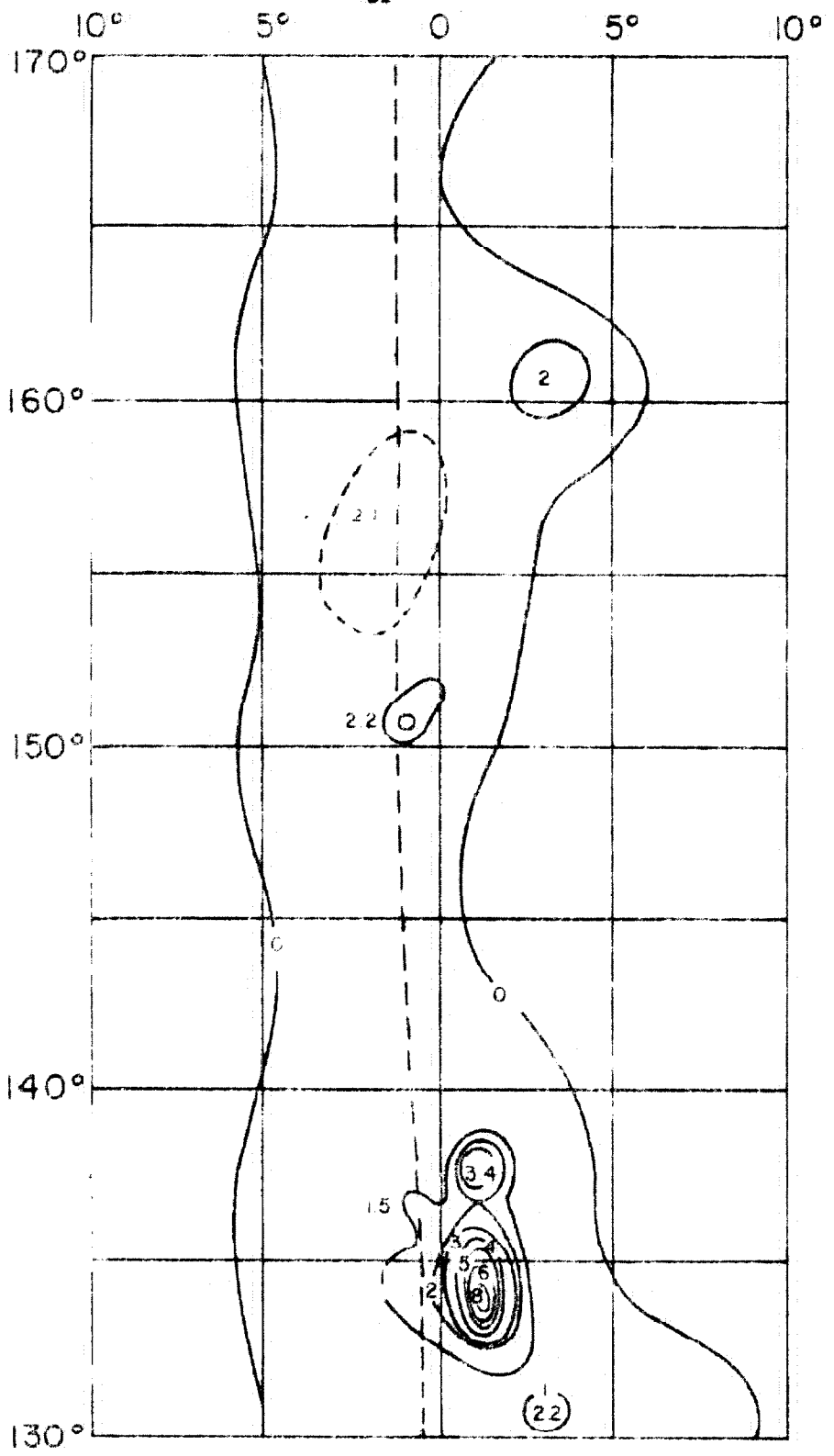

Figure 14. Portion of the contour map of the galactic plane. Contour intervals are 1.85°K in full beam temperature

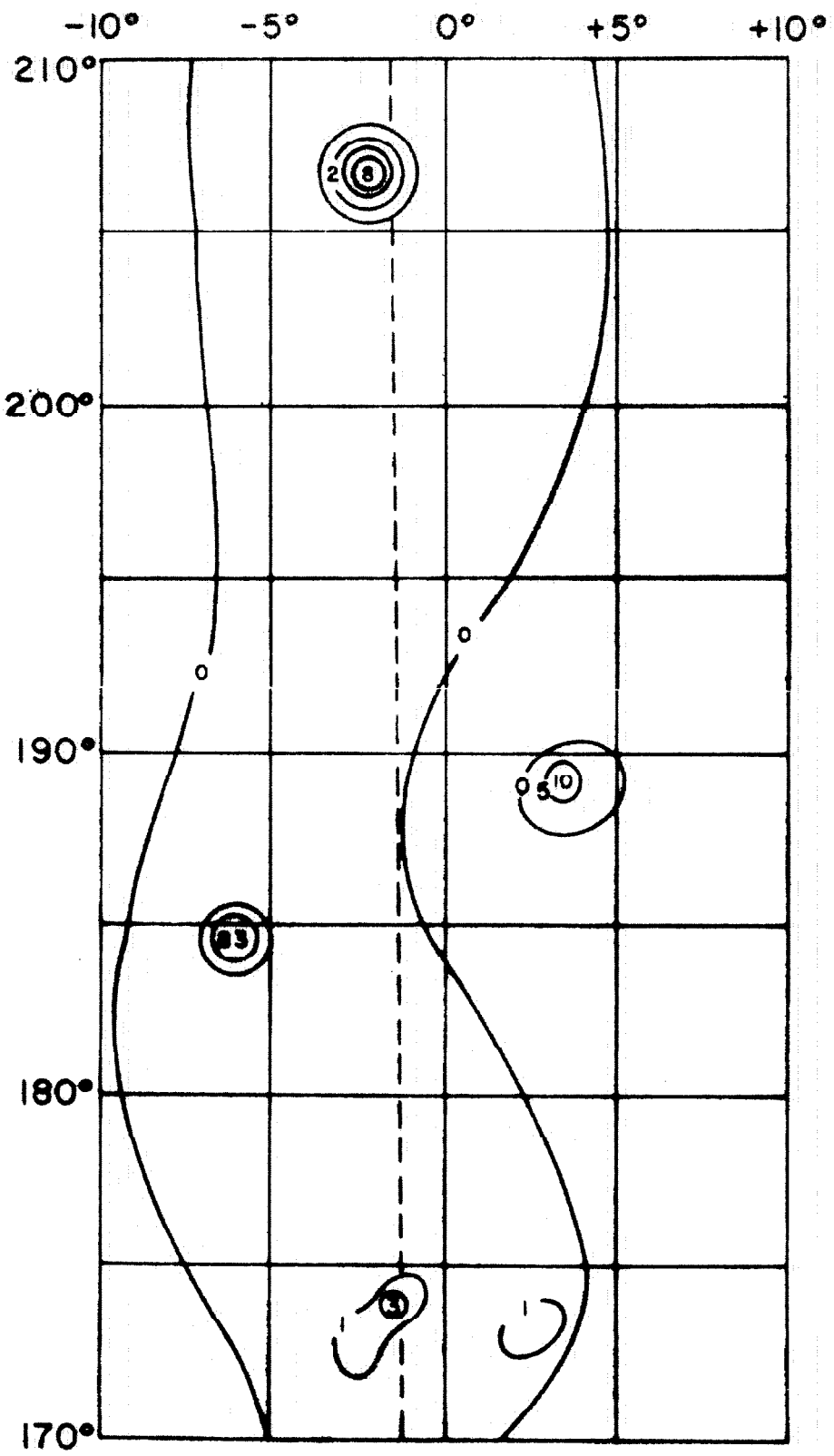

Figure 15. Portion of the contour map of the galactic plane. Contour intervals are 1.85°K in full beam temperature.

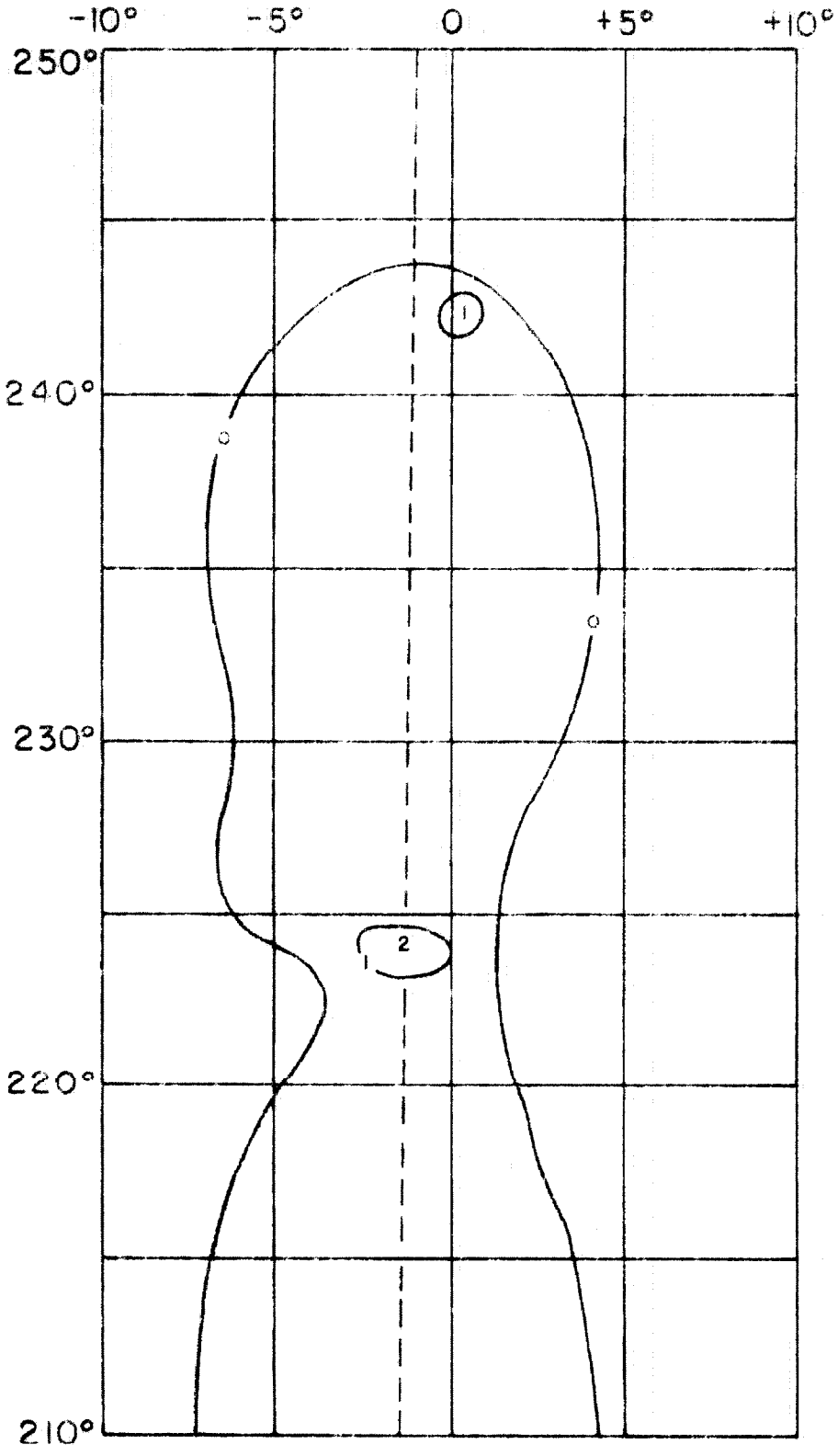

Figure 16. Portion of the contour map of the galactic plane. Contour intervals are 1.85°K in full beam temperature.

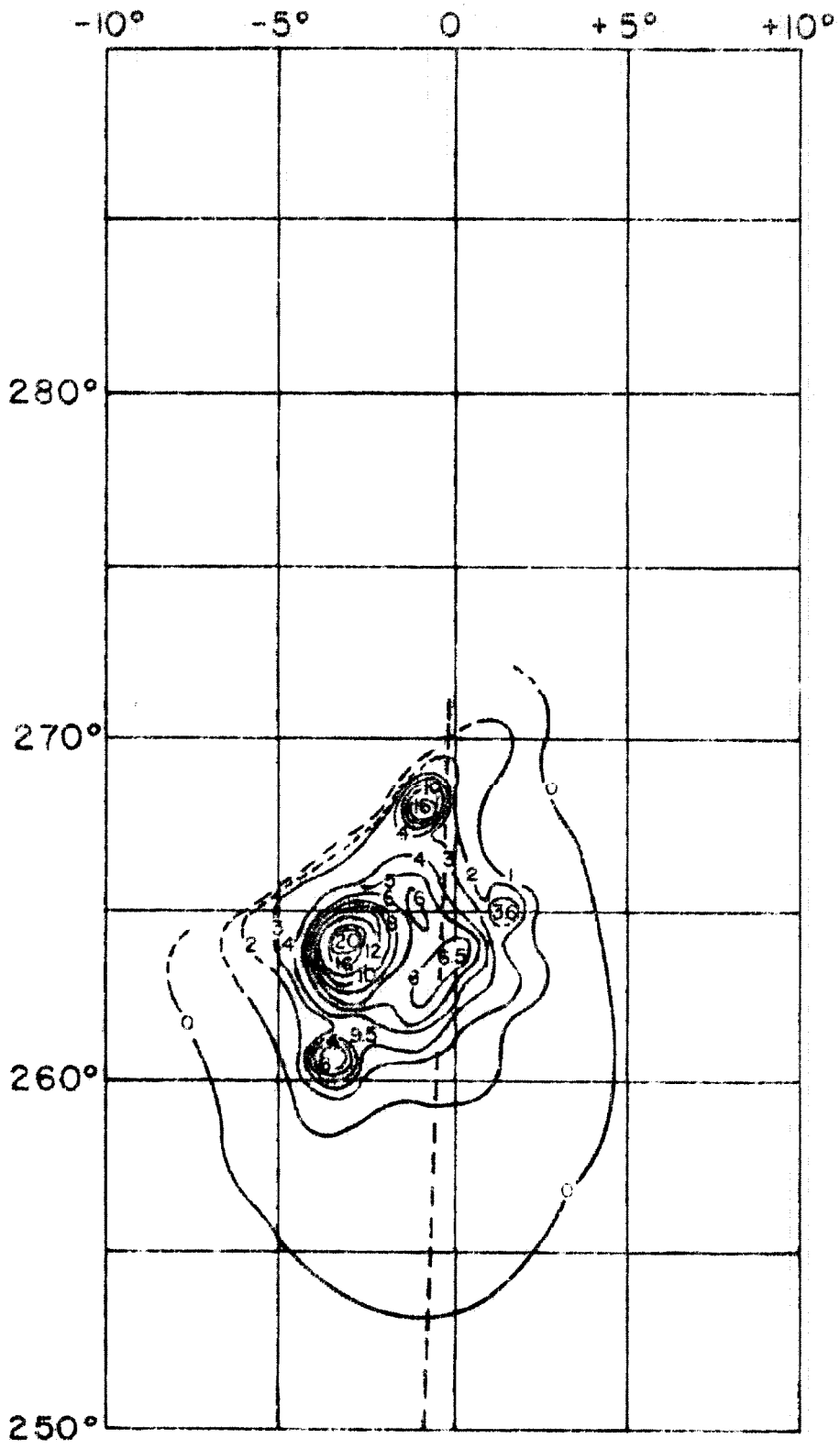

Figure 17. Portion of the contour map of the galactic plane. Contour intervals are 1.85°K in full beam temperature.

APPENDIX II

Table 1. Identification of abbreviated references in figures 5-8.

Abbreviation	Date	Reference
JL	1956	17
AS	1957	8
ML	1958	19
BSS	1954	10
HBH	1953	13
GMH	1957	12
KKM	1954	18
S	1956	9
PT	1957	20
D	1957	11
JPL	1959	27
W	1958	22
DJ	1960	28
GB	1960	30
M	1958	7
HMH	1954	14
Mu	1960	26
SN	1960	25
BM	1960	23
PR	1956	21
KKS	1955	29
HM	1957	16

Table 3. List of discrete sources observed

No.	Name	α (1950)	P.C. (10 Yr.)	δ (1950)	P.C. (10 Yr.)	Peak Response	Flux Density	Single Dish Size	Interferometer Size E-W	Interferometer Size N-S	Spectral Index ±Scatter
1		$23^h59^m.6$ (4)	$0^m.52$	$62^\circ11'$ (2)	3:3	19	26	$0^\circ.5$			
2	W1, K1	23 59.6 (3)	0.52	67 00 (2)	3:3	87	220	$0^\circ.9$			-0.3 ±0.3
3		00 09.6 (4)	0.53	57 47 (4)	3:3	5	?	?			
4	SN 1572	00 22.8 (1)	0.55	63 51 (1)	3:3	57	57		6' x 6'		-0.4 ±0.1
5		00 25 (5)	0.55	55 20 (5)	3.3	6	43	2°			
6	3C 20	00 39.9 (2)	0.57	51 47 (1)	3.3	13	13		0:7x	0:4	-0.5
7	NGC 281	00 50.1 (2)	0.58	56 20 (1)	3.3	16	18	$0^\circ.3$			
8	3C 58	02 01.7 (1)	0.73	64 36 (1)	2.8	33	33		6' x	2:3	+0.5
9	W3&4, K4&5	02 23 (5)	0.73	61 43 (5)	2.7	98	425	$2^\circ.5x1^\circ$			-1.4 ±0.4
10	3C 69	02 34.3 (1)	0.75	58 59 (1)	2.7	6.2	6.2			0:8	-0.9 ±0.2
11	W5, K6	02 48.5 (3)	0.77	60 15 (3)	2.5	50	105	$0^\circ.75$			0 ±0.1
12		04 00.8 (4)	0.75	51 10 (2)	1.7	30	66	$1^\circ.5x0^\circ.25$			
13		04 24 (5)	0.73	47 00 (5)	1.3	15	235	$5^\circ x2^\circ$			
14	HB 9	04 575 (3)	0.73	46 25 (3)	0.8	22	160	2°			+0.4
15	3C 134	05 01.2 (2)	0.68	38 00 (2)	0.8	15	15		0:6x(	0.5+ 0.5)	-1.0
16		05 12.4 (2)	0.67	34 15 (2)	0.7	25	40	$0^\circ.6$			-0.9
17	W8, K9	05 18.7 (2)	0.65	33 26 (2)	0.5	38	66	$0^\circ.7$			+0.2 ±0.4
18	Crab Nebula	05 31.5 (1)	0.53	21 59 (1)	0.4	1030	1030		3:3x	3:3	-0.27
19		05 37.1 (3)	0.60	36 00 (3)	0.3	13	26	$0^\circ.8$			
20	IC 443	06 14.3 (1)	0.60	22 36 (4)	-0.2	129	195	$0^\circ.6$			-0.45±0.1
21	Rosette Neb.	06 29.4 (2)	0.52	04 53 (2)	-0.5	105	342	$1^\circ.2$			+0.1 ±0.1

Table 3. Continued

No.	Name	α (1950)	P.C. (10 Yr.)	δ (1950)	P.C. (10 Yr.)	Peak Response	Flux Density	Single Dish Size	Interferometer Size E-W	Interferometer Size N-S	Spectral Index ±Scatter
22	M 07-12?	07^h04^m (4)	$0^m.47$	$-10°45'$ (4)	-0!8	25	?	$3°-4°$			
23	M 07-215	07 50 (3)	0.42	-26 00 (4)	-1.5	13	18	$0°.5$			±0.2
24	R 51 ?	08 15 (4)	0.38	-36 00 (4)	-1.8	8	?	?			
25	Puppis A, R54 R 105	08 21.4 (2)	0.35	-42 58 (3)	-1.9	116	180	$0°.6$			-0.4 ±0.1
26	Vela x, R56 R 107	08 32.8 (3)	0.35	-45 37 (3)	-2.0	238	1390	$2°.8 \times 2°$			* ±0.0
27	R 57	08 37.6 (5)	0.37	-40 34 (5)	-2.2	13	33	$1°$			±0.4
28	Vela Y, R58 R 108	08 43 (5)	0.35	-43 31 (4)	-2.2	19	130	$2°.5 \times 1°.5$			)
29	Vela Z, R59 R 108	08 45.7 (4)	0.35	-45 03 (5)	-2.2	13	40	$2° \times 0°.5$			)-0.5)
30	R 109	08 48.1 (5)	0.37	-42 15 (5)	-2.2	13	33	$1°$			
31	R 61	08 57.4 (2)	0.35	-47 16 (3)	-2.3	200	250	$0.5° \times 0°.25$			
32	R 62	08 57.8 (3)	0.37	-43 34 (4)	-2.3	33	33		6'		±0.3
33		16 31.3 (3)	0.73	-47 42 (4)	-1.3	172	280	$0°.7 \times 0°.6$			
34	MSH 16-47	16 36.8 (2)	0.73	-46 36 (2)	-1.2	185	340	$1° \times 0°.6$			±0.05
35		16 55.6 (3)	0.70	-40 13 (3)	-1.0	87	134	$0°.6$			
36		17 01 (3)	0.72	-44 20 (3)	-0.8	30	46	$0°.6$			
37	MSH 17-33	17 12.8 (3)	0.68	-38 03 (3)	-0.7	86	195	$1°.5 \times 0°.3$			-0.3
38		17 15.7 (3)	0.68	-39 00 (2)	-0.7	37	37		8'		
39		17 17.7 (2)	0.68	-35 58 (2)	-0.7	170	180		12' x 12'		
40	W 22, UOB 1	17 23 (2)	0.65	-34 21 (2)	-0.5	360	560	$0°.6$			0.0
41	SN 1604	17 28.7 (4)	0.60	-21 36 (4)	-0.5	14	14		2' x 2'		-0.7 ±0.1

Table 3. Continued

No.	Name	α (1950)	P.C. (10 Yr.)	δ (1950)	P.C. (10 Yr.)	Peak Response	Flux Density	Single Dish Size	Interferometer Size E-W	Interferometer Size N-S	Spectral Index ±Scatter
42	Sgr. A	$17^h42^m.9$ (2)	$0^m.63$	$-28^\circ50'$ (2)	-0.3	750	1800	$1^\circ.3 \times 0^\circ.6$			
43	MSH 17-110	17 48 (3)	0.58	-17 15 (4)	-0.2	25	70	1°			
44	W 27	17 57 (4)	0.65	-32 15 (3)	0.0	12	35	1°			
45	W28, MSH 17-216, K 25	17 58 (2)	0.60	-23 30 (3)	0.0	200	300	$0^\circ.8 \times 0^\circ.25$			-0.35±0.05
46	W29, M8, K26	18 00.7 (3)	0.62	-24 21 (2)	0.0	150	159		12'	12'	0 ±0.3
47	W 30, K 27, MSH 18-21	18 01.7 (2)	0.60	-21 39 (2)	0.0	150	210	$0^\circ.5$			-0.05±0.05
48	MSH 18+01	18 04.8 (4)	0.52	00 00 (4)	0.0	12	75	$3^\circ \times 1^\circ$			
49	W31, K28+K29	18 06 (2)	0.60	-20 00 (3)	0.0	150	165		15'	15'	-0.1 ±0.5
50	W 35, K 31	18 15.3 (2)	0.57	-12 00 (3)	0.2	140	280	$0^\circ.8$			-0.1 ±0.1
51	W 37, K 32	18 16.2 (2)	0.57	-13 50 (3)	0.2	100	110		15'	15'	-0.2or±0.5
52	W 38, K 33, M 17	18 17.5 (2)	0.57	-16 18 (2)	0.3	540	500		6'.5	8'	0 ±0.3
53	W39, MSH 18-18, K35	18 23.5 (4)	0.57	-12 30 (4)	0.3	62	210	$2^\circ \times 0^\circ.6$			0.1 ±0.2
54	MSH 18+05	18 27.3 (2)	0.52	00 30 (2)	0.3	19	62	$1^\circ.2$			0.2
55	W 40, K 36	18 28.7 (3)	0.52	-02 12 (3)	0.3	25	25			7'	0 ±0.4
56	W 41, K 38, MSH 18-18	18 31.2 (2)	0.55	-08 45 (3)	0.5	75	80		15'	10'	-0.25±0.05
57	W 42, K 39	18 33.8 (2)	0.53	-07 15 (3)	0.5	50	55		15'	20'	-0.8
58		18 34 (3)	0.57	-12 12 (3)	0.5	12	17	$0^\circ.5$			
59	W 43, K 41	18 44.7 (2)	0.52	-02 06 (3)	0.7	315	1,000	$1^\circ.4 \times 0^\circ.95$			-0.3 ±0.1*
60	W 44, K 42	18 53.6 (2)	0.52	01 18 (2)	0.8	211	240		15'	20'	-0.4 ±0.2

Table 3. Continued

No.	Name	α (1950)	P.C. (10 Yr.)	δ (1950)	P.C. (10 Yr.)	Peak Response	Flux Density	Single Dish Size	Interferometer Size E-W	Interferometer Size N-S	Spectral Index ±Scatter
61	W 45	$18^h54^m.6$ (2)	$0^m.48$	$08^\circ14'$ (3)	0!8	19	22	$0^\circ.3$			
62	W 46	18 55 (3)	0.48	09 15 (3)	0.8	6		?			
63		18 56.4 (4)	0.45	15 37 (4)	0.8	14	150	$2^\circ.5$			
64	W 47, K 44	18 57.7 (2)	0.50	04 04 (3)	0.8	62	87	$0^\circ.5$			-2.2
65	3C 396	19 01.0 (3)	0.50	05 32 (3)	0.8	15	15		4'?x 4'		-0.3
66		19 01.4 (3)	0.47	11 14 (4)	0.8	12	30	1°			
67	3C 397	19 04.6 (2)	0.50	07 12 (4)	0.8	20	20		7' x 3'		-0.2
68	3C 398, W 49, K 46	19 07.9 (2)	0.48	09 02 (2)	1.0	75	75		10' x 3'		+0.2 ±0.1
69	W 50, MSH 19 +01	19 08.4 (3)	0.50	05 04 (3)	1.0	25	50	$0^\circ.8$			-0.2 ±0.1
70		19 13.8 (2)	0.47	11 36 (3)	1.0	37	51	$0^\circ.5$			
71		19 16 (5)	0.50	02 05 (5)	1.1	2	12?	2°?			
72		19 15.9 (3)	0.50	06 00 (3)	1.1	19	80	$1^\circ.5$			
73	W 51, K 48	19 20.7 (2)	0.47	14 04 (2)	1.2	320	450	$0^\circ.5$			+0.6
74		19 22.8 (2)	0.45	16 00 (3)	1.2	50	60	$0^\circ.35$			
75		19 39 (5)	0.50	02 30 (5)	1.3	13	?	2°			
76	W 55	19 40 (2)	0.43	23 06 (3)	1.4	8	9	$0^\circ.3$			
77		19 44 (4)	0.42	24 45 (4)	1.5	13	22	$1^\circ x 0^\circ.3$			
78		19 44.8 (3)	0.40	28 00 (3)	1.5	12	15	$0^\circ.35$			
79		19 46 (5)	0.48	09 30 (5)	1.5	13	320	4°			
80	W 56, K 49, UOB 5	19 51.8 (2)	0.38	33 00 (3)	1.6	47	130	$1^\circ.1$			-1.6

Table 3. Continued

No.	Name	α (1950)	P.C. (10 Yr.)	δ (1950)	P.C. (10 Yr.)	Peak Response	Flux Density	Single Dish Size	Interferometer Size E-W	Interferometer Size N-S	Spectral Index ±Scatter	
81	Cyg. A	$19^h57^m.7$ (1)	$0^m.35$	40°36' (1)	1!7	2190	2190		(0!7+0!7)	x0!7	-0.79	*
82	W 58, UOB 8	19 59.2 (2)	0.38	33 24 (2)	1.7	31	34		15'	x 10'	+1.8	
83	UOB 7	19 59.4 (3)	0.38	35 00 (3)	1.7	13	?	$0^\circ.4$				
84	W 59	20 05 (3)	0.38	34 06 (3)	1.7	13	?	1°-2° x 1°				
85		20 12 (2)	0.38	36 05 (3)	1.8	36	40	$0^\circ.3$				
86	UOB 12	20 14.3 (3)	0.38	33 55 (3)	1.8	13	60	$1^\circ.5$				
87	UOB 10	20 14.3 (3)	0.37	37 03 (4)	1.9	10	10		4'	x 4'		
88	W 63, UOB 13	20 16.6 (5)	0.33	45 00 (5)	1.9	50	170	$1^\circ.5$x1°				
89		20 19.5 (2)	0.35	40 52 (2)	1.9	63	160	1°				
90a	UOB 15a(W64)	20 19.7 (2)	0.42	37 02 (3)	1.9	19	65	$1^\circ.5$x1°				
b	UOB 15b	20 23.4 (2)	0.38	37 02 (3)	2.0	5	?	?				
91a	W 66, K 52	20 21 (3)	0.37	40 00 (2)	2.0	250	800	$1^\circ.8$x$0^\circ.6$			-1.3	
b	W 65	20 18 (3)	0.37	39 00	1.9	14	19	$0^\circ.5$				
92	W 68b	20 27 (3)	0.35	41 10 (3)	2.0	31	31?	P?				
93	W 70, UOB 17	20 30.4 (3)	0.35	43 48 (3)	2.0	60	90	$0^\circ.6$x$0^\circ.5$				
94	UOB16?, W69?	20 32 (2)	0.37	39 30 (2)	2.0	63	180	$1^\circ.2$			-1.2	
95	W 71, UOB 19	20 32.7 (2)	0.33	46 58 (3)	2.0	50	80	$0^\circ.6$			-0.4?	
96	W 75, UOB20, K 54	20 37.5 (3)	0.37	41 55 (4)	2.2	160	1200	2°				
97	HB 21	20 44.7 (2)	0.32	50 32 (2)	2.2	48	180	$1^\circ.4$			-0.06	
99	Cyg. Loop	20 48.2 (5)	0.42	29 30 (5)	2.2	33	265	$2^\circ.5$x2°			-0.1 ±0.1	

Table 3. Continued

No.	Name	α (1950)	P.C. (10 Yr.)	δ (1950)	P.C. (10 Yr.)	Peak Response	Flux Density	Single Dish Size	Interferometer Size E-W	Interferometer Size N-S	Spectral Index ±Scatter
100	W 80, UOB 23	$20^h52^m.5$ (5)	$0^m.35$	44°09' (5)	2:3	75	430	$2^\circ x1^\circ.5$			-0.3 ±0.3
101		21 07.6 (3)	0.33	49 34 (3)	2.3	17	24	$0^\circ.5$			
102		21 10.6 (3)	0.32	52 16 (2)	2.5	38	95	1°			
103		21 20 (5)	0.37	44 03 (5)	2.6	13	94	2°			
104a		21 26.2 (3)	0.35	50 33 (3)	2.6	19	43	$0^\circ.9$			
104b		21 37.7 (3)	0.35	50 17 (3)	2.7	15	38	1°			
105	HB 22	21 35.4 (5)	0.30	57 30 (5)	2.7	28	240	$2^\circ.5x2^\circ$			-1.4?
106		22 18.5 (3)	0.37	55 58 (3)	3.0	31	190	$4^\circ x1^\circ$			
107		22 22.6 (5)	0.33	63 17 (5)	3.0	21	75	$1^\circ.3$			
108		22 56.3 (3)	0.40	62 20 (3)	3.2	25	39	$0^\circ.6$			
109		23 00.3 (4)	0.42	58 45 (2)	3.3	25	63	$1^\circ.5x0^\circ.5$			
110	Cas. A	23 21.2 (1)+	0.45	58 32 (1)+	3.3	3120+	3120+		3:5x3:5		-0.77

NOTES TO TABLE 3

Comments about identification, size, etc.

1) The declination agrees closely with a bright filamenty circular ring of 0.5^{o} diameter which van den Berg (private communication) suggests is a supernova remnant. There is faint, uniform Hα emission south of an indentation in the southern part of the ring. The ring is faintly visible on the blue plate.

2) Sharpless 171, NGC7822, emission nebula. A low level extension of radio object to the NW corresponds to a bright loop NW of NGC7822.

3) May not exist.

4) Remnants of SN1572 (Tycho's). Fine structure ~ $2'$.

5) May not exist.

6) This small diameter source may be extragalactic.

7) Sharpless 184, NGC 281, em. neb.

8) Possibly extra-galactic.

9) Sharpless 190, IC1795 and 1805, emission nebulae.

10) May be extra-galactic.

11) Sharpless 199, IC1848, emission nebula.

12) Approximately 20% of the flux is concentrated in a core about $3'$ in diameter. IC1491, Sharpless 206. The radio contours are extended to the east, apparently by a faint, but probably highly obscured emission region, Sharpless 209. The association with this object is strengthened by the very close agreement in declination on the declination scans.

13) Some fine structure. This radio source may be divided into two or more parts (observations inadequate). Some long filaments appear on both O and E plates about $0^{\circ}.75$ south of the center of the source. Patchy absorption in the area. Bolton suggests this may be a supernova remnant.

14) Supernova remnant.

15) Double source. Located in an obscured region. May be extragalactic.

16) IC405, Sharpless 229.

17) IC410, Sharpless 236. Extends over 2 or 3 degrees, but has central a concentration of about $18'$ diameter.

18) Some central concentration.

19) Extended to the west. About 25% of the flux concentrated in a core $\leq 4'$ in a diameter (N. S.). Radio source covers the positions of Sharpless 231, 232, 233, and 235.

20) IC443. Some fine structure. Supernova remnant.

21) Some fine structure.

22) Incomplete observations. Probably associated with Sharpless 296 and 292, with possible contributions from 293, 295, and 297. Radio contours seem to follow the shape of 296 and 292.

23) Sharpless 311.

24) NGC2568 (NGC declination has a 1° error). Emmission nebula. Extended, but size observations inadequate.

25) Supernova remnant. Fine structure $\leq 15'$.

26) Stromlo 16. Supernova remnant similar to Shain 147. Long filamentary structure with heavy obscuration.

27) Stromlo 14. Emission nebula.

28) Probably part of 26.

29) Probably part of 26.

30) Stromlo 17. Emission nebula.

31) Stromlo 23. Emission nebula. Concentration of about 35% of flux in a 2' core.

32) Stromlo 20. Emission nebula. Strong concentration in a core.

33) Position close to NGC6164-5. An unusual planetary nebula (52) or H II region (53). 6' in extent. Considerable obscuration and other emission in the region with some filamentary structure. Fine structure $\leq$ 15' in diameter.

34) Fine structure $\leq$ 15' in diameter.

35) Stromlo 56. Radio position near the eastern edge which is bounded by high obscuration.

36) The radio position is in a region of about 1^{o} in diameter with lower than average absorption for the plate. May not exist.

37) Extended to S. E. Has a core $<$ 10' N. S. x $<$ 15' E. W. containing around 30% of the flux. In a heavily obscured region. Near the edge of an emission region. (Sharpless 51?).

38) Complex structure with components $<$ 3' E. W., $<$ 5' N. S. Located between a patch of emission (S4?) and an association of 5 patches within 4'.

39) Radio position adjacent to Sharpless 8. Components $\leq$ 6' N. S.

40) Sharpless 11. Fine structure $<$ 10'.

41) Evidence of fine structure.

42) 25% ± 5% of peak response is in a core of 3' ± 0!5 diameter. Total flux listed corresponds to a "central part."

43) Bright, obscured section of the Milky Way with no features coincident with the radio source.

44) Bright, obscured section of the Milky Way.

45) Located on a patch of emission about 25' in diameter near M20. Complex structure with components ≤ 7' N. S., ≤ 5' E. W.

46) M8. Components less than 4'.

47) In a heavily obscured region off the edge of Sharpless 34.

48) Obscured region. Nothing visible the size of this source.

49) Located in the middle of a region of increased obscuration about 0!5 in diameter. Components < 7'.

50) Sharpless 54, NGC6604. Fine structure around 7' N. S.

51) Sharpless 49. Radio position near edge with heavy obscuration.

52) M17. Radio position with RA of dark lane. Structure < 4'.

53) Located on a highly obscured lane. South part contains a highly obscured H II region.

54) Highly obscured region. Slight indication of H II region behind.

55) Possibly heavily obscured emission nebula.

56) Obscured region.

57) Fine structure < 9' N. S. Located on a local patch of obscuration. Evidence of an H II region at northern edge of the obscured patch.

58) Located on a local increase in obscuration around 15' in diameter. May not exist.

59) About 25% of peak flux in a 3' core. Spectral index given is correct if 960 Mc/s size is incorrect (i. e. it is actually a point

source).

60) Small source superimposed on an extended object.

61) Heavily obscured region.

62) Heavily obscured region.

63) Some absorption.

64) Fine structure $\leq 10'$ N. S. Very heavily obscured.

65) Single dish intensity uncertain. Source may have larger diameter component surrounding the $4'$ core. Heavily obscured region. Possible extra-galactic.

66) Some absorption.

67) E. W. components $< 2'$. Appears on Westerhout's survey, but not listed. Heavy obscuration. Possibly extra-galactic.

68) Complex structure E. W. Two principal components with relative intensity 1.6 ± 0.3:1. Diameter $4' \pm 1'$. Separation $13' \pm 2'$. Possibly extra-galactic.

69) Heavily obscured.

70) Fine structure $\leq 10'$. Highly obscured.

71) Some absorption.

72) Fine structure $\leq 10'$ N. S. May not exist. Some absorption.

73) Obscured region. Extended to north. Fine structure $< 15'$.

74) Obscured.

75) May not exist.

76) Sharpless 86, NGC6820. Radio position near border with heavy obscuration.

77) Between Sharpless 87 and 88. Obscuration. Fine structure $< 2'$ N. S. Probably core of $\leq 0.'5$ containing 10% of peak flux.

78) Sharpless 92

79) Some absorption.

80) Emission and absorption.

81) Two 0.'7 sources with intensity equal within 25% separated by 1.'59 along position angle 106°. Spectral index seems to be a function of frequency. Best straight line fit is given. Extra-galactic.

82) Fine structure < 4'. Lies between Sharpless 99 and 100, two small emission regions of diameter 5' and 4', separation 10'.

83) Fine structure < 8'. Lies in a heavy patch of absorption next to Sharpless 101. The error in the radio position is such that the true position could be on Sharpless 101.

84) An area with wisps of emission and considerable obscuration.

85) Wisps of emission, obscuration.

86) Wisps of emission, obscuration.

87) Complex. Some components < 1'. Emission and absorption.

88) High obscuration. Wisps of emission.

89) In a dense patch of obscuration. Extension of 91. Fine structure < 10'.

90 a and b) Spotty emission and obscuration.

91a) Radio position lies on the dense absorption band across the γ-Cygni nebula (Sharpless 108).

91b) Lies on a bright patch southwest of the γ-Cygni nebula.

92) Components < 4'. Lies in a region of patchy emission and absorption.

93) Next to a heavily absorbed edge of an emission region.

94) Extension of 90? Lies in a region of dense absorption.

95) Whisps and clumps of emission.

96) Some emission showing in a region with dense obscuration.

97) Supernova remnant.

99) Cygnus loop. Supernova remnant.

100) Radio emission centered on a dark absorption band across Sharpless 117, NGC7000.

101) 25% of flux in a $1'$ core. Position given is position of core. Obscuration.

102) Obscured.

103) Probably faint, extended emission nebula, Sharpless 119. The radio position differs by $3^{\prime}.5$ in RA and $19'$ in Dec. from the center of Sharpless 119, but due to the size and weakness of the source could be in error by that amount.

104a) Obscured.

104b) Radio position approximately central to the outer faint parts of Sharpless 124, a highly obscured emission nebula.

105) Sharpless 131, IC1396. Brightest radio emission northwest of center of optical and radio extremes near an absorption patch with very bright edges.

106) May be extended north to Dec. = 61°. Lower part is possibly Sharpless 132.

107) Separated from Sharpless 140 by a very heavy absorption band.

108) Probably Sharpless 155. Radio center is located over heavy obscuration in the nebula.

109) In a large region of faint emission.

110) Supernova remnant.

Table 4. Meaning of the error symbols of Table III and credits for Table III.

Meaning of the error symbols	
(1)	± 2'
(2)	± 4'
(3)	± 10'
(4)	± 20'
(5)	> 20'

Source Number	Credit
4	1, 2, 4
6	1, 2, 4
7	4
8	1, 2, 4
10	2, 5
14	4
15	1, 2, 4
16	3
17	3
18	1, 2, 4
19	3
20	4
21	4
32	1
38	1
41	1
52	1
67	1
68	1
81	1, 4
87	1
97	4
99	6
110	1, 2, 4

Credits:

(1) EW Diameter measured by Moffet (44).
(2) NS Diameter measured by P. Maltby (45).
(3) Contours for these 3 sources taken from unpublished work of Moffet.
(4) Position and intensity taken from Harris and Roberts (31).
(5) Position taken from CTC list (Matthews personal communication).
(6) Spectrum and intensity taken from D. E. Harris thesis (47).

Table 5. Flux densities of the sources at various frequencies, in $Wm^{-2}(c/s)^{-1}$.

Number	Kuzmin 3125 Mc/s	Lynds 1400 Mc/s	Westerhout 1390 Mc/s	CTB 960 Mc/s	HB 185 Mc/s	3C 159 Mc/s	Mills or Rishbeth 85.5 Mc/s	Rishbeth 23 Mc/s
2	160	185	130	220				
4	30	37		57	170	110		
6				13		30		
8				33		13		
9		274	210	425				
10		3		6.2		23		
11	100		97	105				
14				160	80			
15				15		85		
16		29		40				
17	70	46	62	66				
18	[790]		900	1030				
20	100		174	195			550	
21	300		210	342			225	
23				18			10	
25				180			630	800
26				1390			1340	360
27				33			13	
28 & 29				170				600
32				33			16	
34				340			287	
37				195			420	
40			565/390	560				
41	10			14		58	92	
42			2950/1050	1700			3760	
43				>70			26+	
44			113	>35				
45			290	300			740	
46	160		210/150	159				

Table 5. Continued

Number	Kuzmin 3125 Mc/s	Lynds 1400 Mc/s	Westerhout 1390 Mc/s	CTB 960 Mc/s	HB 185 Mc/s	3C 159 Mc/s	Mills or Rishbeth 85.5 Mc/s	Rishbeth 23 Mc/s
47	180		194	210			210	
48				12/75			28	
49	80+		57	165				
50	220		210	280				
51	180		210	110				
52	650		855/570	500				
53	230		89	210			127	
54				62			41	
55	40		50	25				
56			60	80			134	
57			40	55				
59	215		270	315/1,000				
60	140		154	240		680	460	
64			36	87				
65				15		24.5		
67				20		29		
68	90		60	75		43		
69			36	50			69	
73			570	450		25		
76			20	9				
80			69	130				
81	630		1530	2190	5700	8600		
82			69	34				
84			69	13				
88			81	170				
90a			20	65				
91a			480	800				

Table 5. Continued

Number	Kuzmin 3125 Mc/s	Lynds 1400 Mc/s	Westerhout 1390 Mc/s	CTB 960 Mc/s	HB 185 Mc/s	3C 159 Mc/s	Mills or Rishbeth 85.5 Mc/s	Rishbeth 23 Mc/s
91b			36	19				
93			89	90				
94			154	180				
95		50	69	80				
96			218	160/1,200				
97				180	200			
100		337	444	430				
105		116		210	50			
109		20		63				
110	1450	2500	2500	3120	9250	13,000		

Table 6. Total temperature and thermal component of disk radiation

ℓ^{II}	b^{II}	T(85.5)	T(960)	α	T_T(85.5)	T_T(960)
355.3	-3.63	5,500	17	2.41	330	2.2
	-2.63	6,600	20.7	2.40	475	3.2
	-1.63	8,900	27.7	2.40	605	4.1
	-1.13	9,400	31.8	2.36	1,150	7.7
	-0.63	10,200	38.6	2.31	1,940	13.2
	-0.13	12,300	50.8	2.27	2,830	20.8
	0.37	14,000	50.4	2.33	2,030	14.1
	0.87	14,000	42.2	2.41	630	4.4
	1.37	12,300	34.4	2.43	310	2.3
	2.37	9,000	26.4	2.42	360	2.5
	3.37	6,800	21.4	2.40	490	3.4
	4.37	6,400	18.1	2.45	0	0
	5.37	4,700	15.8	2.37	610	3.9
4.3	-4.58	5,200	19.3	2.33	1,040	6.7
	-3.58	6,800	21.7	2.40	480	3.4
	-2.58	7,600	25.3	2.38	780	5.2
	-1.58	10,400	31.6	2.41	550	3.8
	-1.08	13,100	36.2	2.45	0	0
	-0.58	15,000	42.8	2.44	150	1.5
	-0.08	15,600	48.2	2.40	870	6.4
	0.42	14,300	47.8	2.39	1,000	7.5
	0.92	12,800	41.4	2.37	1,280	8.6
	1.42	11,900	35.2	2.42	420	3.2
	2.42	9,000	26.2	2.42	360	2.4
	3.42	7,100	19.6	2.46	100	-0.6
	4.42	4,500	16.2	2.34	810	5.2
11.3	-4.53	5,700	20.4	2.35	890	5.8
	-3.53	6,000	21.1	2.33	1,140	7.4
	-2.53	6,600	23.8	2.34	1,110	7.3
	-1.53	7,800	28.5	2.33	1,380	9.2
	-1.03	9,100	33.4	2.32	1,680	11.1
	-0.53	10,900	41.3	2.31	2,010	14.1
	-0.03	12,900	47.7	2.32	2,070	14.5
	0.47	13,100	44.6	2.36	1,440	10.0
	0.97	11,500	37	2.38	1,000	7.0
	1.47	9,400	31.1	2.37	1,000	6.8
	2.47	5,800	23.3	2.30	1,420	9.6
	3.47	4,400	18.6	2.33	960	6.3
	4.47	3,150	16.2	2.20	1,570	10.6
20.8	0	11,300	40.9	2.33	1,770	12.3

Table 6. Continued

ℓ^{II}	ℓ^{II}	T(85.5)	T(960)	a	T_T(85.5)	T_T(960)
26.3	-4.53	4,700	14.2	2.40	350	2.4
	-3.53	5,500	16.8	2.39	500	3.4
	-2.53	6,100	20.1	2.36	840	5.5
	-1.53	7,200	24.2	2.36	960	6.4
	-1.03	8,300	28.2	2.35	1,190	8.0
	-0.53	8,900	36.7	2.27	2,280	16.7
	-0.03	9,200	43.6	2.21	2,980	22.9
	0.47	9,300	42.0	2.42	2,780	21.3
	0.97	8,000	31.5	2.29	1,880	13.4
	1.47	6,800	26.3	2.30	1,600	11.0
	2.47	5,300	19.9	2.31	1,220	8.2
	3.47	4,900	18.0	2.32	1,060	7.0
	4.47	4,100	16.8	2.28	1,230	8.5
	5.47	3,340	15.0	2.21	1,580	10.2
32.3	0	8,600	33.8	2.29	1,400	14.0
36.3	-2.58	3,900	14.2	2.32	870	5.7
	-1.58	5,300	17.0	2.37	660	4.3
	-1.08	6,300	19.8	2.38	660	4.4
	-0.58	7,800	25.6	2.34	1,250	7.9
	-0.08	8,700	29.5	2.35	1,220	8.0
	0.42	8,400	28.8	2.35	1,180	8.0
	0.92	7,300	24.6	2.35	1,070	7.1
	1.42	6,200	20.3	2.36	840	5.6
	2.42	4,800	13.7	2.42	220	1.5
	3.42	3,900	11.4	2.41	250	1.7
	4.42	3,400	10.4	2.39	340	2.2
42.3	0	7,200	27	2.31	1,520	10.4